Chapter 8

Me-DLC films deposited by pulsed-DC reactive magnetron sputtering

Chapter 8 – Me-DLC films deposited by pulsed-DC reactive magnetron sputtering

8.1. Deposition parameters

A series of Me-DLC thin films has been deposited onto RF-biased substrates by reactive magnetron sputtering of metal (Mo, Nb, Ti, W) targets in a gas mixture of Ar and CH_4. Actually, the deposition technique can be considered as a hybrid between magnetron sputtering and plasma-enhanced CVD. Ar was needed in these processes in order to sputter the targets, whereas the growth turned into reactive due to CH_4 injection. In fact, this is the precursor of the carbon content in the deposited films. Moreover, RF-biasing of the substrate-holder increases the energy of bombarding ions. The aim of varying the relative CH_4 flow consisted of adjusting the metal content in Me-DLC samples.

Prior to the Me-DLC films deposition, some metal-free carbon samples were prepared by RF-PECVD to optimize the technological parameters of deposition. The considered variables were the pressure, the bias voltage and the CH_4 dilution. Figure 8.1 shows the evolution of the deposition rate of DLC films as a function of the self-bias voltage in pure CH_4 atmospheres at 0.2, 5 and 10 Pa of pressure. The consideration of higher pressures is discarded because a dusty regime is reached, where generation of particulates that contaminate growing films takes place.

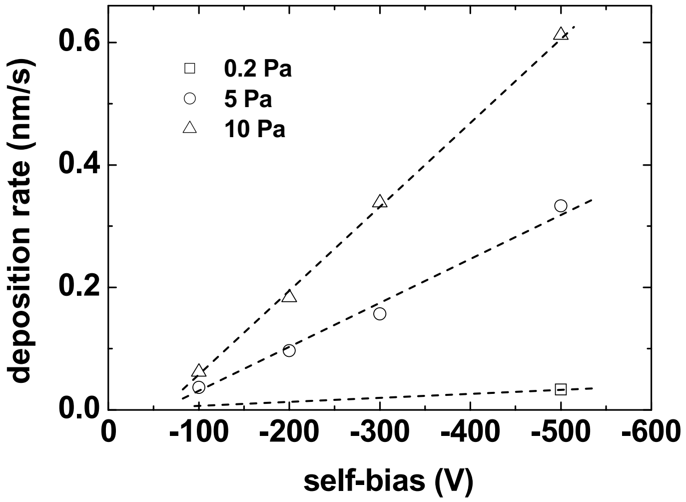

Figure 8.1: Deposition rate of DLC films as a function of cathode self-bias in RF-PECVD in a CH_4 glow discharge.

An monotonous increment of the growth rate is observed as voltage values increase. It is supposed that all curves collapse in the origin because the plasma is switched-off at null self-bias voltage and no deposition occurs. The enhancement of the growth rate at higher pressures is justified by the presence of more reactive species in the discharge.

An important property of thin films influencing their adherence to substrate is intrinsic stress. Figure 8.2 plots DLC film stress vs. self-bias. A stress of -4 GPa is measured at 0.2 Pa, which is a typical value for hard DLC films. However, it supposes a drawback for the film stability on a given substrate if the thickness of the coating exceeds a certain limit, as explained in the introductory part. Stresses registered at higher pressures are the most indicated for the performance of Me-DLC films as protective coatings.

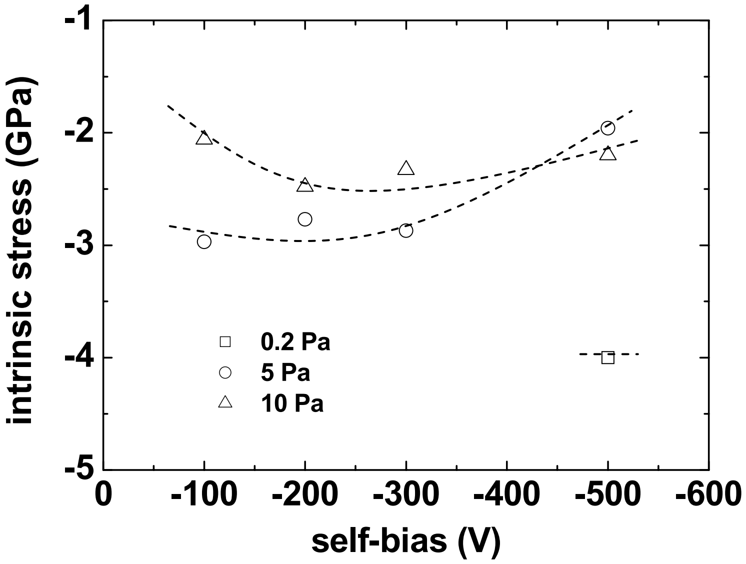

Figure 8.2: Intrinsic stress of DLC films as a function of cathode self-bias in RF-PECVD in a CH_4 glow discharge.

In the next step, we will determine some process parameters. The gas pressure of 0.2 Pa is discarded due to the low deposition rate and extremely high stress of the resulting films. The deposition of Me-DLC films will be carried out at 5 Pa and -200 V for the reasons exposed next. We have chosen this working pressure because, though samples prepared at 10 Pa are more rapidly deposited, sputtering processes are more efficient at lower pressures. On the other hand, a characteristic property of carbon films with diamond-like properties is an elevated stress. Thus, samples prepared at high self-bias are withdrawn. The election of -200 V self-bias coincides with high hardness of methane-deposited DLC measured elsewhere [Jiang X., 1989].

To finish this preliminary study, an additional series of DLC films has been deposited at different gas mixtures of CH_4 and Ar: 25%, 50% and 75% relative CH_4 flow, *R*, which is defined as:

$$R = \frac{\phi(CH_4)}{\phi(CH_4) + \phi(Ar)} \tag{8.1}$$

where ø(CH_4) and ø(Ar) are the fluxes of methane and argon, respectively. The adding of Ar flux in the plasma has kept intrinsic stress to -2.5 GPa in the whole range, whereas deposition rate has decreased from 0.097 nm/min to 0.055 nm/s at 25% CH_4 rate. This decrease is a consequence of the minor concentration of the precursor, CH_4, and of the film erosion introduced by Ar. This value of 25% was finally taken to prevent from a major poisoning of targets.

Sputtering targets were placed on a water-cooled cathode equipped with a magnetron. The electric signal was driven by a pulsed-DC supply operating at 100 W of power, 100 kHz of pulse frequency and 70% of duty cycle. The election of such parameters provided a stable waveform signal, which was monitored by an oscilloscope. Previous to the deposition of each series of Me-DLC, the metal targets were cleaned by means of Ar plasma. The goal of this ion attack was to remove the carbon layer deposited onto the metal targets after every process. Furthermore, a cleaning protocol was performed to the substrates before deposition in order to remove the silicon oxide layer from c-Si surface. It consisted of a bombarding process with Ar ions from plasma at 0.3 Pa pressure and -800 V self-bias during 5 min.

The only technological variable used in this study was the relative CH_4 flow, *R*. It was varied between 0% and 25%. In the first case, we deposited pure metal (Mo, Nb, Ti or W) films; at 25%, we obtained carbon-rich coatings. The variation of *R* between these extreme values provided Me-DLC films with a wide range of metal concentrations. The total gas flow was set to 40 sccm, and a valve located in the evacuation line quenched the gas flow in order to keep a constant pressure of 5 Pa.

8.2. Deposition rate

The first step in the characterisation of a thin film is the evaluation of its deposition rate. From figure 8.3 one can see that the growth rate of Me-DLC films depends on the used metal and on the CH_4/Ar ratio, and that it generally increases with the relative methane flow. This behaviour is contradictory with the fact that sputter rates of metals drop dramatically when compounds are formed on the targets [Ohring M., 2002]. However, this can be understood as a consequence of removing of low adhesive carbon aggregates by Ar etching [Maharizi M., 2001]. As expected, deposition rate of Me-DLC at 25% is greater than for DLC. The reason is the contribution of metal sputtering added to the initial presence of CH_4 gas.

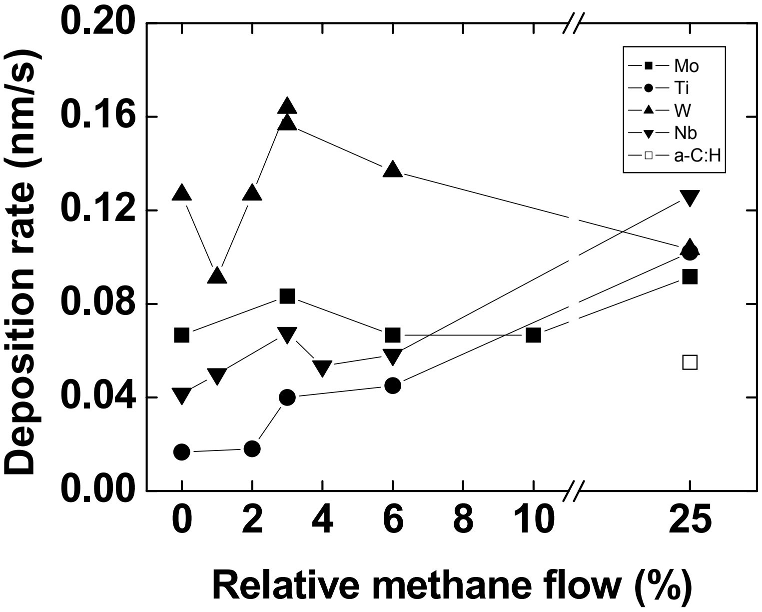

Figure 8.3: Deposition rate vs. relative methane flow of Me-DLC films deposited by reactive magnetron sputtering with pulsed power.

W-DLC films arise as the structures with fastest deposition, showing a peak of 0.16 nm/s at $R = 3\%$. The decrease observed between 0% and 3% might come from the reactivity of CH_4 with W in the target or in the gas phase. Nevertheless, the rate diminishes from this maximum tending to the deposition rate of DLC. The velocities corresponding to Mo- and Nb-DLC show values lower than 0.10 nm/s, therefore they are lower with respect to W-DLC case. Ti-DLC exhibits the lowest rate, whose minimum corresponds to the metallic sample.

Now we try to relate the observed deposition rates with data of sputtering yields of table 8.1, which shows the sputtering yield data for metals sputtered by noble gas ions at 500 eV. A rough estimation of the yield corresponding to our depositions is possible when inspecting the figure 8.4, where the evolution of the target bias as a function of CH_4 dilution is plotted. The variation of the bias is produced due to a process of target poisoning, i.e. the covering of the target surface by a carbonaceous layer. The fact that W target bias is located between -600 and -900 V, supports the fact that W-containing films present the highest deposition rate, because among Mo, Nb, Ti and W, the sputter yields of W targets show the highest sensitivity to either or the energy of the sputtering species.

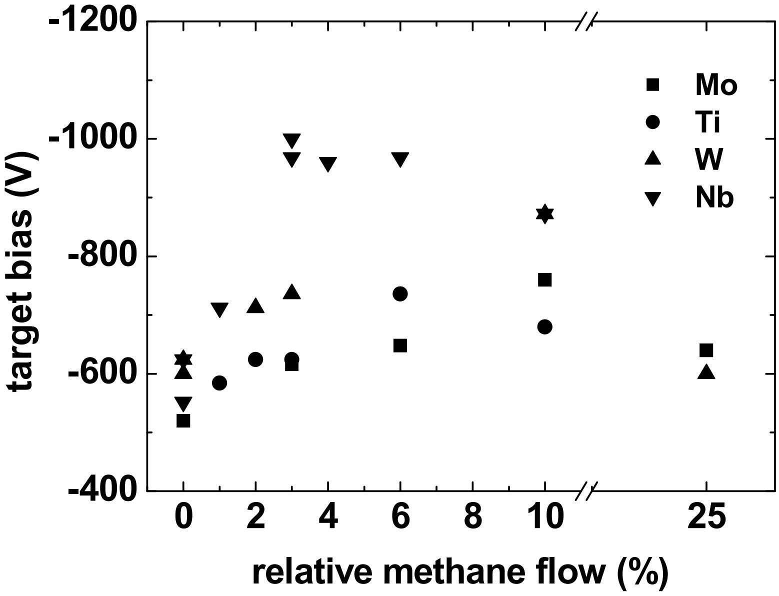

Figure 8.4: Target bias during pulsed-DC reactive magnetron sputtering of different metals.

metal \ gas	He	Ne	Ar	Kr	Xe
Al	0.16	0.73	1.05	0.96	0.82
Ti	0.07	0.43	0.51	0.48	0.43
Ni	0.16	1.10	1.45	1.30	1.22
Cu	0.24	1.80	2.35	2.35	2.05
Nb	0.03	0.33	0.60	0.55	0.53
Mo	0.03	0.48	0.80	0.87	0.87
Ag	0.20	1.77	3.12	3.27	3.32
Ta	0.01	0.28	0.57	0.87	0.88
W	0.01	0.28	0.57	0.91	1.01

Table 8.1: Sputtering yield data for metals at gas energy of 500 eV (atoms/ion) [Ohring M., 2002].

8.3. Chemical composition vs. relative methane flow

Here we show data concerning to the metal-to-carbon ratio in Me-DLC films and we discuss the relationship of such data with the CH_4 dilution. To this end, the Me-DLC structures were either analysed by XPS or EPMA techniques. Note that chemical composition is reported without considering hydrogen content, since the intensity of its signal lies below the detection threshold in both methods.

The metal concentration of the samples was calculated from the analysis of XPS signals corresponding to C(1s), Ti(2p), Mo(3d), W(4f) and Nb(3d) core levels using the standard sensitivity factors of the instrument. Figure 8.5 displays the metal content vs. the relative CH_4 flow during deposition process. These data correspond to the composition on the surface, because the scan depth of this technique comprehends only a few Å. Deeper layers of the sample can be analysed by performing successive sputtering attacks. However, a short-time (1 min) sputtering has been developed previous to each analysis in order to remove impurities from the surface.

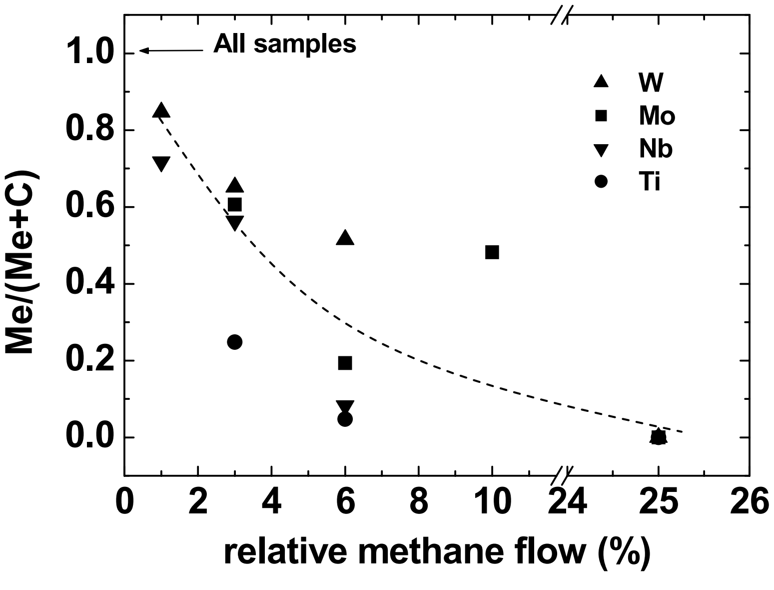

Figure 8.5: Relationship between the relative methane flow in the deposition processes and the chemical composition determined by XPS. All the samples are carbon-free at *R*=0.

All the films are metallic at null CH_4 dilution. When small fluxes of CH_4 are injected into the chamber, the metal concentration curve presents a saturation regime: it decreases from 100% with a rate that depends on metal. The metallicity of W-DLC samples decreases smoothly, whereas Ti-DLC films achieve quickly a value below 30% at 3% of CH_4 concentration. Above approximately 10% CH_4 injection, the Me-DLC films experience a faster decrease in metal content. This second regime owes to the lack of chemical homogeneity in the samples deposited at higher CH_4 dilution, as it is explained below.

Depth-profile chemical composition of Me-DLC films measured by SIMS is shown in figure 8.6. These results are not quantitative; they only provide a qualitative mapping of element abundance because sensitivity factors are unknown. It is remarkable that the metal-rich films present homogeneous composition, as shows the constant intensity of SIMS signals corresponding to a Mo-DLC (R=3%) plotted in figure 8.6(a). However, the samples prepared at higher CH_4 flows have lost this uniformity. Figure 8.6(b) shows SIMS profile of a Mo-DLC film deposited at 25% CH_4 ratio. The C signal is uniform and the most intense of all the constituents. The Mo signal is almost zero. Nevertheless, the composition varies roughly in the interfacial region close to the substrate. The Mo content suffers a prompt increase, defines a peak and goes rapidly to zero. Meanwhile, the C concentration diminishes roughly until its signal is practically extinguished. One can model this sample as a carbon film deposited onto an ultra-thin Mo-containing layer. That is the reason why C-rich films show zero metal content when analysed by XPS. What happens is that XPS provides information from the film surface. Although metal atoms exist within the sample, they are so deeply located that the X-rays probe is not able to reach them, and therefore their abundance may be underestimated.

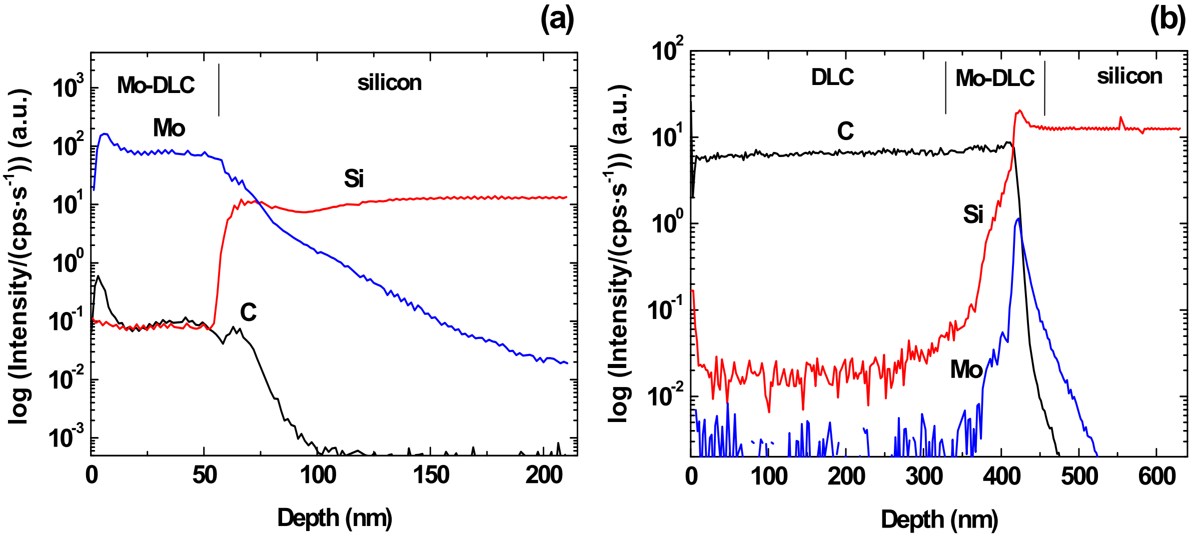

Figure 8.6: Depth-profile chemical composition of Mo-DLC films measured by SIMS: (a) R=3% (MoDLC 020627-2) and (b) R=25% (MoDLC 020701-1).

The lack of homogeneity registered in the C-rich films reflects the history of film deposition. It is well known that sputtered targets suffer a surface poisoning when they are exposed to a reactive environment. Our plasma is composed by two gases, Ar and CH_4. The Ar gas is used for target sputtering. The CH_4, which also feeds the glow discharge, is the gas precursor of the DLC phase deposited on c-Si substrates, but the species coming from this gas are also expected to impinge on the target. As soon as the process starts, a carbon film grows on the target surface due to the presence of the CH_4 gas. This growth mechanism competes with the erosion effect due to Ar until that both mechanisms, i.e. depositing and sputtering, reach a dynamical equilibrium. Thus, the thickness of this layer is limited by the Ar-to-CH_4 ratio, *R*, as shown in figure 8.7.

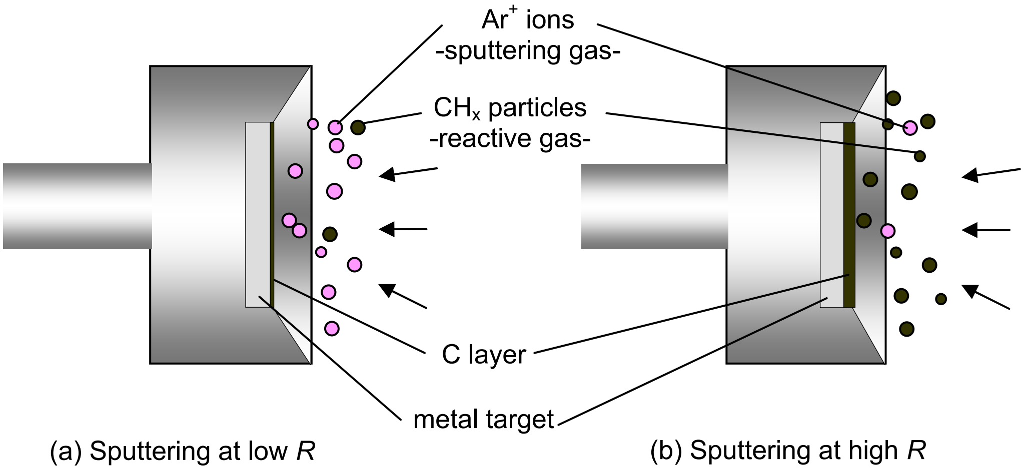

Figure 8.7: Target poisoning during reactive magnetron sputtering at (a) low and (b) high *R* values.

If the relative CH_4 abundance is low, this equilibrium is achieved soon and the metal target is weakly poisoned, i.e., it is contaminated by a thin C layer (figure 8.7(a)). On the other hand, a high CH_4 flow leads to a thick coating on the target already since an early stage of sputtering (figure 8.7(b)). Then, a Me-DLC deposition takes place in non-stationary conditions because target composition varies: firstly, a metal-rich target provides a metal-containing thin layer stacked onto the substrate, and secondly, a DLC film is stacked onto the metallic layer due to the covering of the target by carbon. As described in the experimental section (chapter 3), a cleaning protocol consisting in sputtering process only with Ar was made previously to each series, in order to reset the initial conditions.

Another technique employed to obtain the composition of the Me-DLC films is EPMA. Figure 8.8 shows a comparative between XPS and EPMA results corresponding to W- and Nb-DLC samples with different metal concentrations. The data obtained from both techniques match with a maximal discrepancy of 15%. As the microprobe method includes bulk information and XPS gives account only of surface composition, such small discrepancy indicates that the Me-DLC films are in general homogeneous. The unique exception comes from Me-DLC films deposited at 25% CH_4 ratio. Therefore, a 10% of this gas in plasma could be considered a limit value in order to prepare uniform coatings.

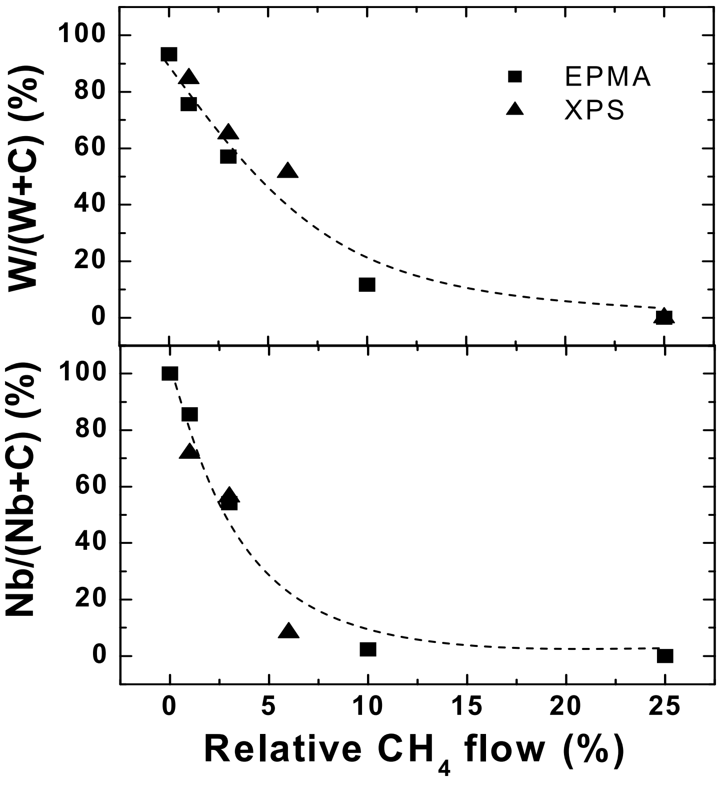

Figure 8.8: Comparative of EPMA and XPS results corresponding to W- and Nb-DLC samples.

8.4. Transmission electron microscopy: growth patterns

In this section, an investigation on the nanostructure of the Me-DLC films is reported. According to the criterion of Musil [2000] described in chapter 1, these films show the structure of nanocomposite (type 3). The information has been extracted from bright- and dark-field TEM micrographs taken to cross-section samples with different chemical composition.

Each added metal confers to the Me-DLC films a characteristic nanostructure [Corbella C., 2005a]. Moreover, relevant structural differences in samples prepared with a given metal appear when composition is varied. Different growth patterns have been distinguished depending on the sputtered metal.

8.4.1. W-DLC: DLC films structured by means of W addition

The columnar structure of a W film (R=0%) is evidenced by the cross-section TEM image in figure 8.9(a). The column height defines the film thickness, whereas grain boundaries that contain void regions limit the column width. Figure 8.9(b) shows a detail of the columns grown in the W film, and figure 8.9(c) is a dark-field micrograph of the same region. The latter image shows the distribution of crystals with a determined orientation within the film. As shown by the tracks performed by Bragg's reflections, the crystals were oriented according to the direction defined by the columns and they formed elongated grain domains of about 20 nm width. The SAED diffractogram inset in figure 8.9(a) accounts for the presence of a polycrystalline phase with preferred orientation, since dots, indicative of an oriented growth, appear diffused.

Figure 8.10 corresponds to a W-DLC film with 75% at. W (R=2%). The columns are still well defined and side-branches appear attached to them, which conform a dendritic-like structure. Figures 8.10(a) and 8.10(b) account for this structure. The SAED diffractogram inset in figure 8.10(b) presented only a diffuse ring surrounded by a weak halo. This pattern corresponds to a very amorphous material, effect that can be attributed to the structural transition from columnar crystals, typical of W, to nano-crystalline inclusions. All the analysed W-DLC samples exhibited this crystalline configuration. Even W-DLC with the highest W concentration (85% at.) showed the same pattern. Thus, the crystallinity of W films was significantly reduced with a small addition of C.

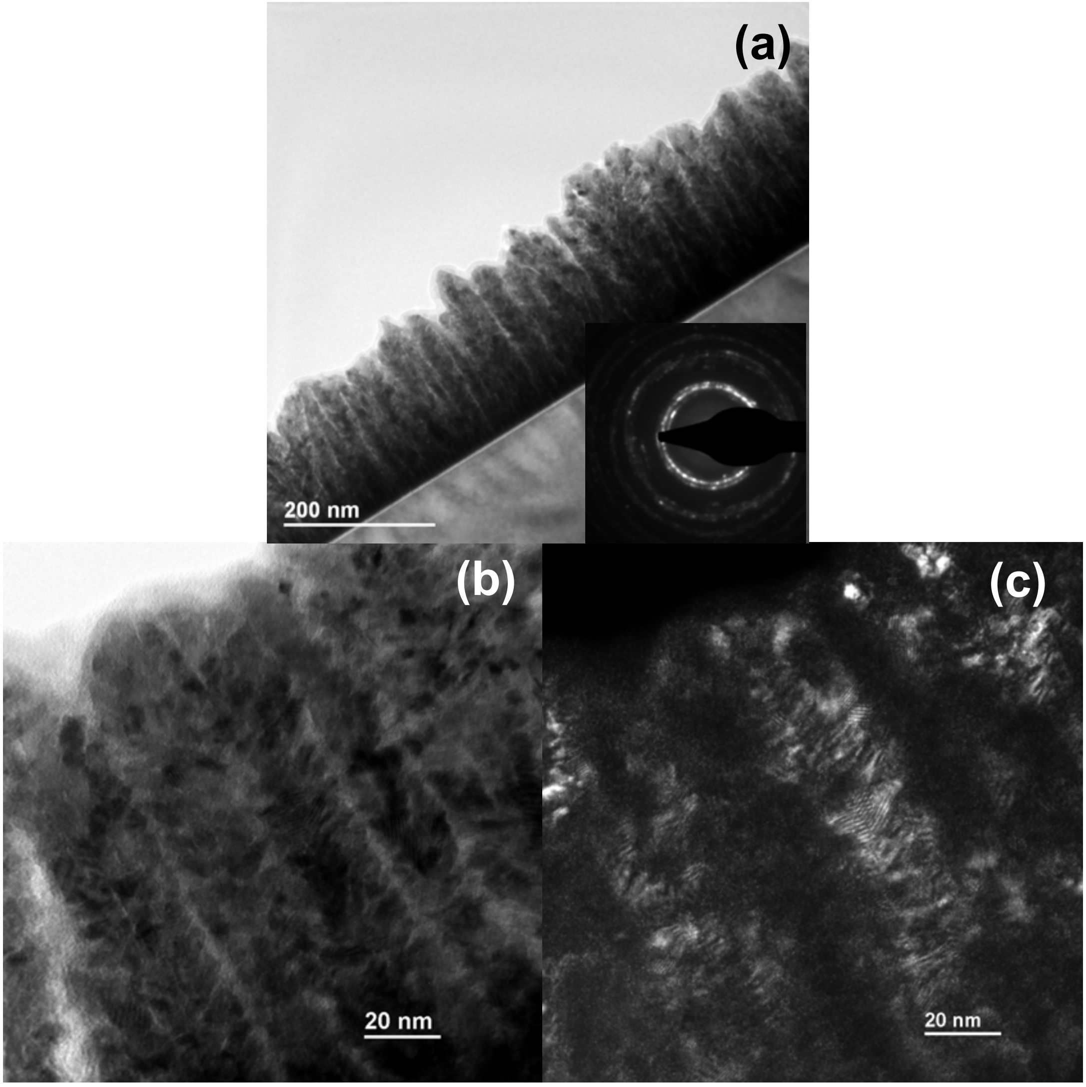

Figure 8.9: Cross-section TEM micrograph of a W film (W 030616-1) with a SAED inset (a), where a detail near the surface is shown in bright- (b) and dark-field (c). The SAED diffractogram accounts for the presence of a polycrystalline phase.

Figures 8.11(a) and 8.11(b) are EELS mappings filtering W and C signals, respectively. The darker zones have a deficit of the mapped element, so it can be inferred that most of C lies in the space between columns. Although EELS is a suitable technique to obtain film composition, only qualitative analysis has been possible in Me-DLC. Indeed, true content of carbon is altered due to the plasma cleaning prior to each EELS analysis (see chapter 4).

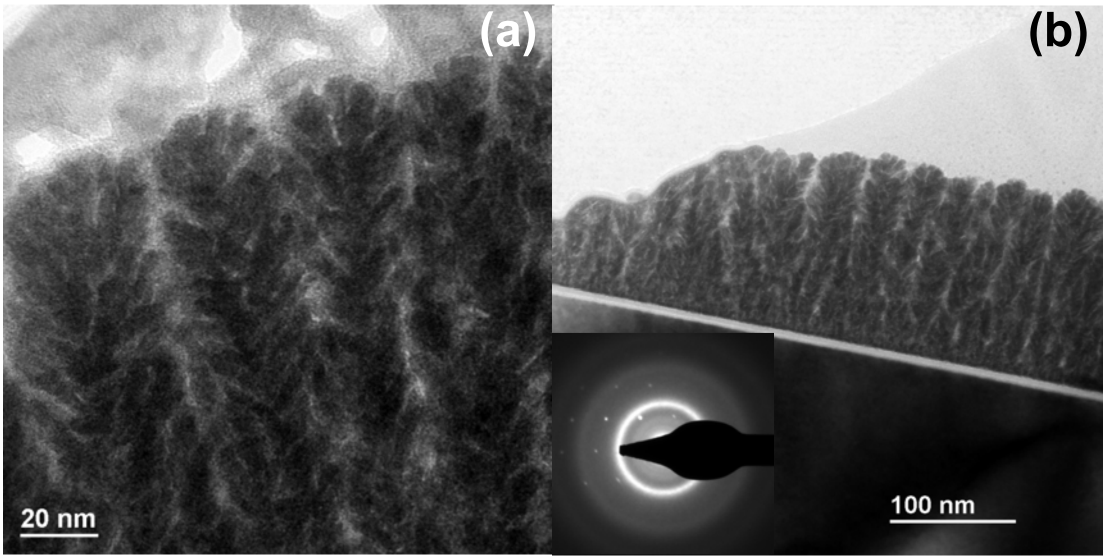

Figure 8.10: TEM micrographs of W-DLC 75% at. W (WDLC 030121-1) showing the dendritic-like structure.

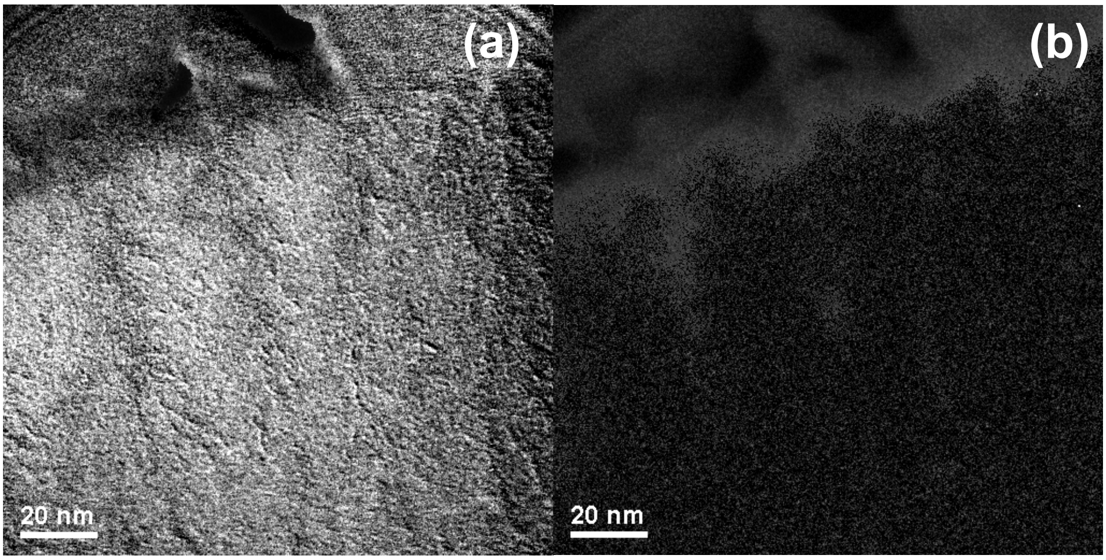

Figure 8.11: EELS analysis of W-DLC films (WDLC 030121-1) provided W (a) and C (b) mappings.

Figure 8.12 is a high-resolution TEM (HRTEM) image, in which crystallites of nanometric size (nano-crystallites), smaller than the crystal domains of W film, are observed to grow within W-rich regions.

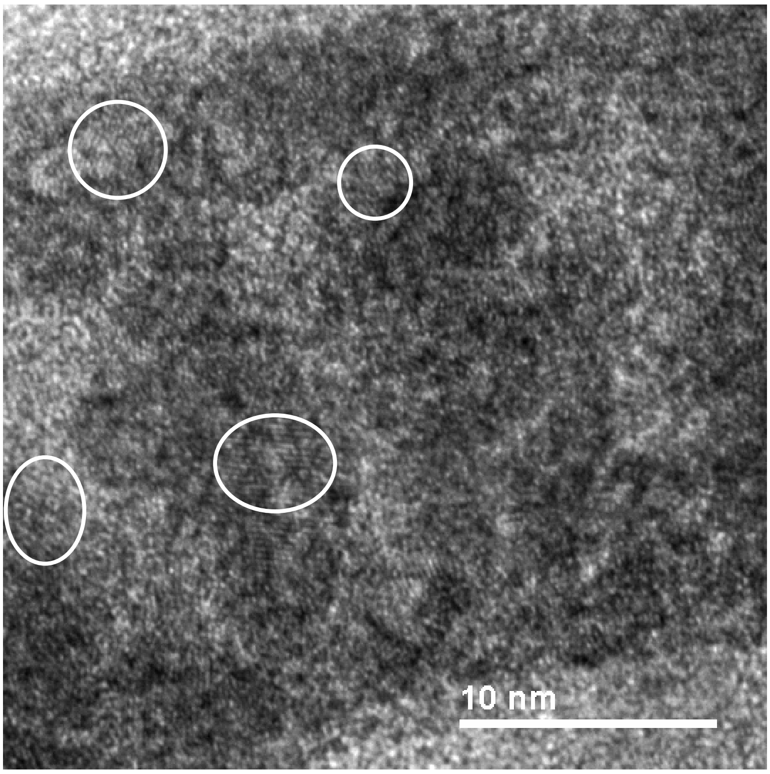

Figure 8.12: HRTEM image of a W-DLC film (WDLC 030121-1) with some circled nano-crystallites.

Figure 8.13 shows TEM images of a series of W-DLC films with a metal concentration that decreases gradually. Dendrites appeared more defined at lower W abundances, probably due to an effect of phase segregation induced by the incorporation of carbon. Indeed, C-rich regions were shifted from the axis of the columns to the grain boundaries, as show C and W mappings in figure 8.11. This segregation could also inhibit the crystalline growth, so it would explain the trend to amorphization of W-DLC films. The sample with 50% at. W shows a structure with side-branches that appear more packed. In this case, the concentrations of C and W could reach a critical value such that phase segregation mechanism may not be active any longer. DLC films do show an extrapolation of the dendritic structure, in which side-branches disappear and a disordered amorphous C matrix without grain boundaries remains, as shows the DLC sample in figure 8.13(f).

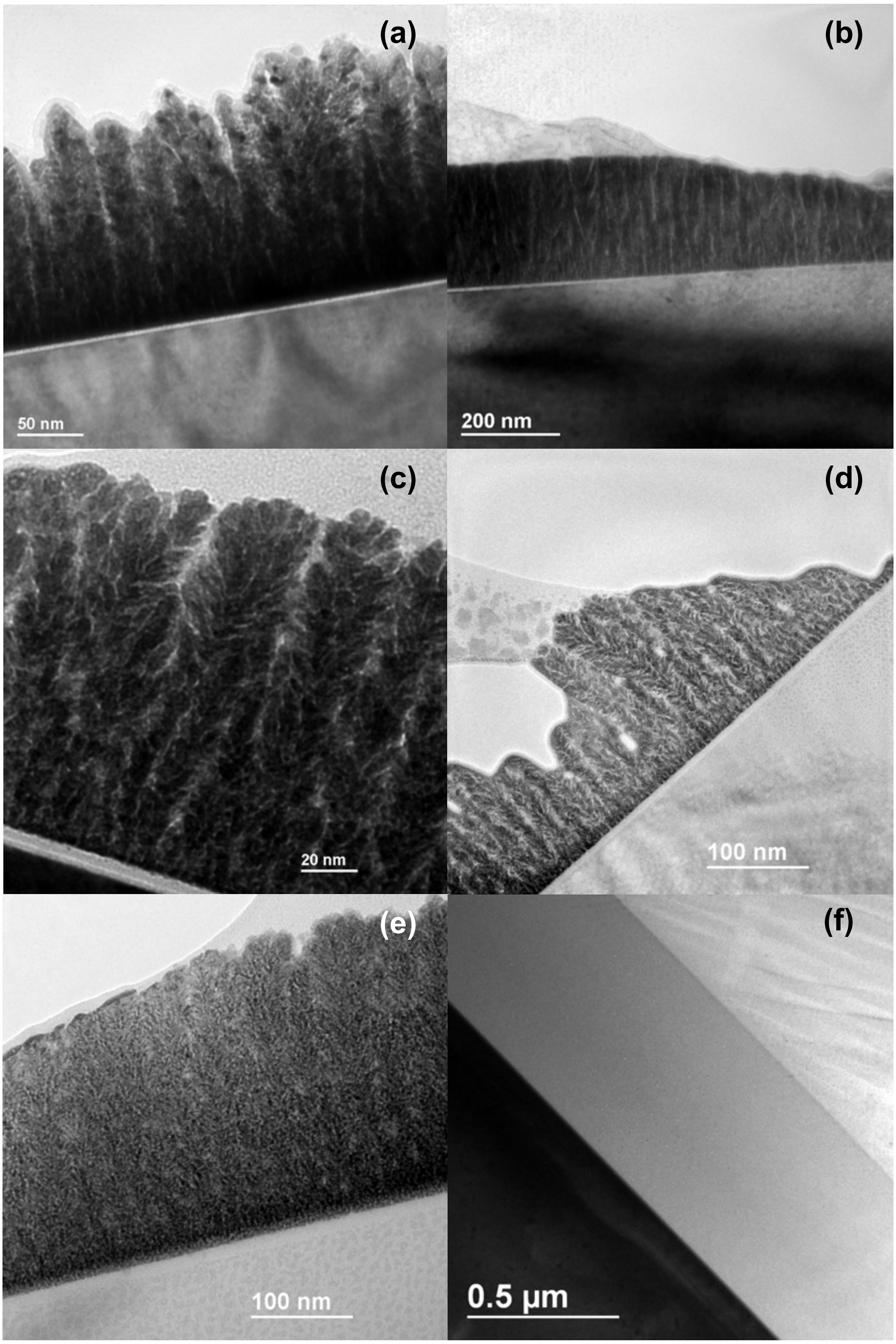

Figure 8.13: Cross-section TEM images corresponding to the W film (W 030616-1) (a), and W-DLC samples with 85% (WDLC 020716-1) (b), 75% (WDLC 030121-1) (c), 65% (WDLC 030121-2) (d) and 50% (WDLC 030120-2) (e) at. W. The last figure is an amorphous DLC film (f).

The surface topography is influenced by the columnar growth of W-DLC films. Indeed, AFM scans reveal a roughening in surface of W-DLC films compared with the case of flat DLC films. This result has been quantitatively displayed by RMS surface roughness, as described in section 8.6.

8.4.2. Ti-DLC: spontaneous formation of nanometric multilayers

Figure 8.14 shows cross-section TEM micrographs and SAED images corresponding to Ti-DLC films prepared at *R* values of 0, 2, 3 and 6%. The Ti film has a columnar structure, whereas a non-regular multilayer structure is inferred from the plano-parallel alternating contrast modulation observed in the TEM images. The first layer after the substrate is the thickest one, and the periodicity suffers a smooth decrease as the layers approach the surface. Furthermore, the modulation is lost in the outmost layers, where material mixing may occur.

This lack of periodicity points to a growth process with non-stationary conditions, due to the target poisoning by CH_4 explained in section 8.3. In the extreme case, the C-richest sample (*R* = 25%) consisted in a C film stacked onto a thin Ti-rich interlayer, as revealed by depth-profile composition analysis by Secondary Ion Mass Spectrometry (SIMS).

Figure 8.15 shows a detail of a Ti-DLC sample with 25% at. Ti and the substrate. Compositional mappings corresponding to this region were obtained by means of EELS analysis. Ti and C signals appear alternatively arranged in layers, as display figures 8.16(a) and 8.16(b), indicating a diffused compositional modulation throughout the film: C-rich and Ti-rich regions are stacked forming nanometric multilayers.

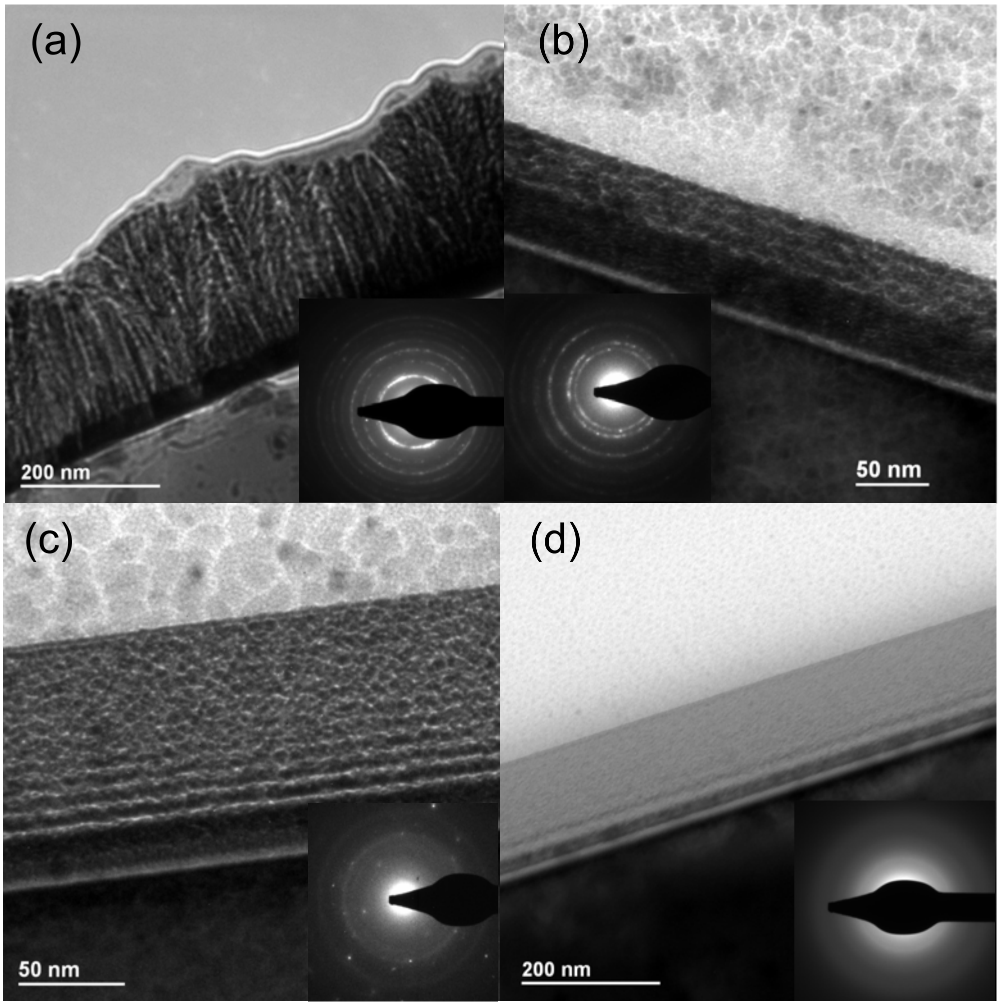

Figure 8.14: Cross-section TEM micrographs of Ti-DLC films with: 100% at. Ti (a), 60% at. Ti (TiDLC 030127-1) (b), 25% at. Ti (TiDLC 030610-2) (c), and 5% at. Ti (TiDLC 030128-1) (d). The corresponding SAED patterns are located below each image.

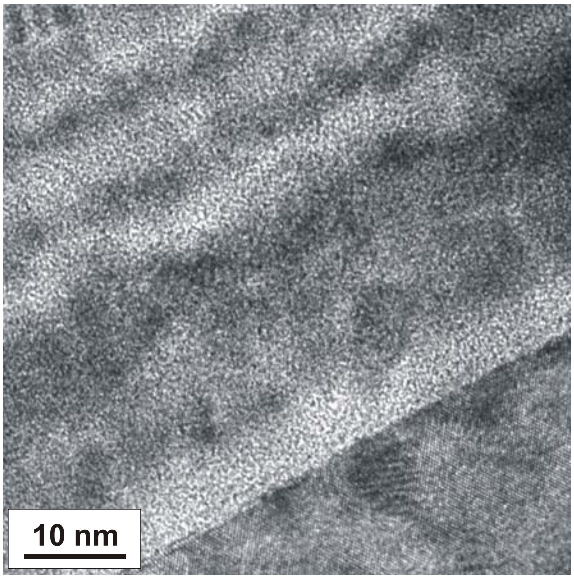

Figure 8.15: TEM image showing the multilayer structure of a Ti-C film with 25% at. Ti (TiDLC 030610-2).

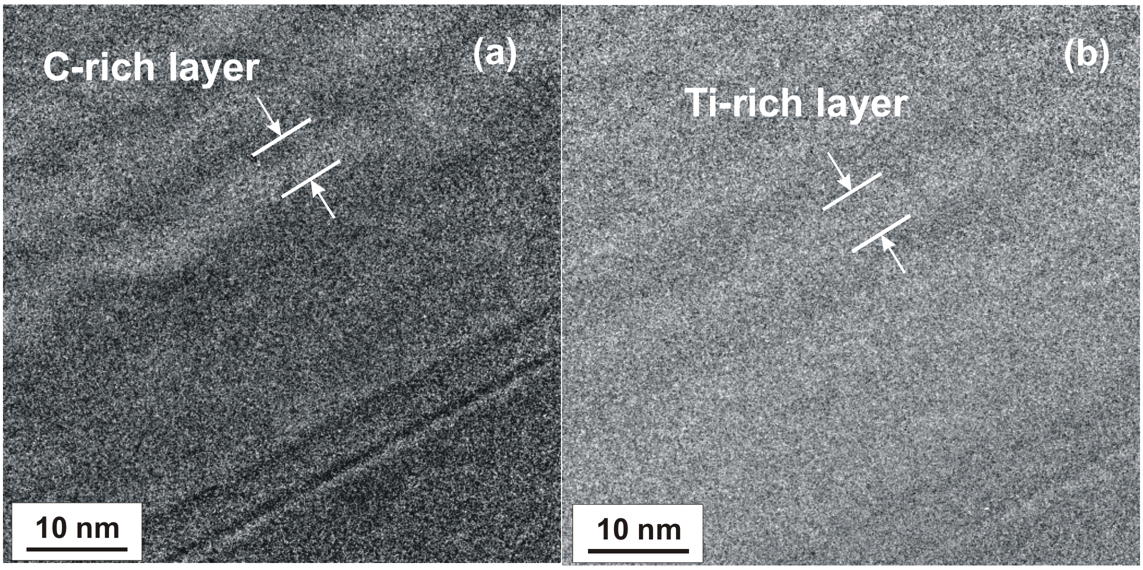

Figure 8.16: EELS mappings of the same region highlight (a) C-rich and (b) Ti-rich layers.

The periodicity of the multilayer was measured by SAED technique. A superlattice diffraction spectrum was obtained, whose profile is shown in figure 8.17. The multilayer wavelength is provided by analysing the distribution of diffraction maxima/minima in the superlattice diffractogram, as performed in chapter 7. An average bilayer period of 8.2 nm was calculated, which is consistent with that observed in figures 8.14 and 8.15.

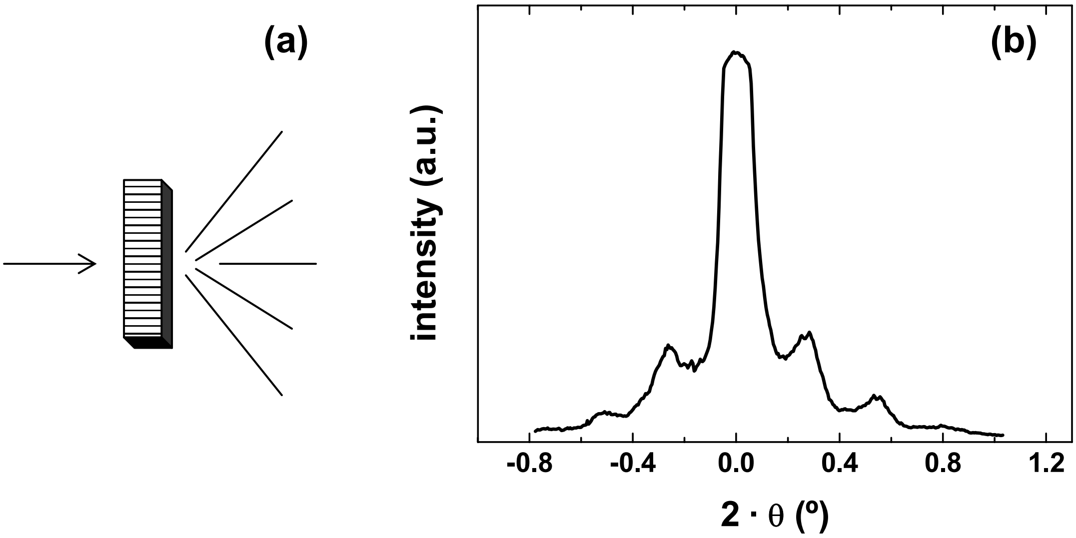

Figure 8.17: (a) Scheme of a multilayer acting as a diffraction lattice and (b) profile of the superlattice SAED diffractogram of the Ti-DLC film with 25% at. Ti (TiDLC 030610-2).

Three diffraction rings were detected from SAED spectra corresponding to the sample with 60% at. Ti, indicating that this film lodges randomly oriented crystals (figure 8.14). These rings owe to the presence of TiC crystallites. Ti-DLC film with 25% at. Ti showed less intense diffraction maxima, and the sample with 5% at. Ti exhibited a diffuse ring, indicative of its amorphous character. Hence, SAED patterns showed an evolution from a polycrystalline to amorphous state as the metal content in Ti-DLC films decreased. These results have been reproduced in data extracted from XRD measurements (section 8.5).

The dimensions and distribution of crystallites have been observed by HRTEM analysis. Figure 8.18 shows a HRTEM image corresponding to the Ti-DLC film with 25% at. Ti. The presence of such crystallites is highlighted by a Moiré pattern, which results from the superposition of several crystalline patterns.

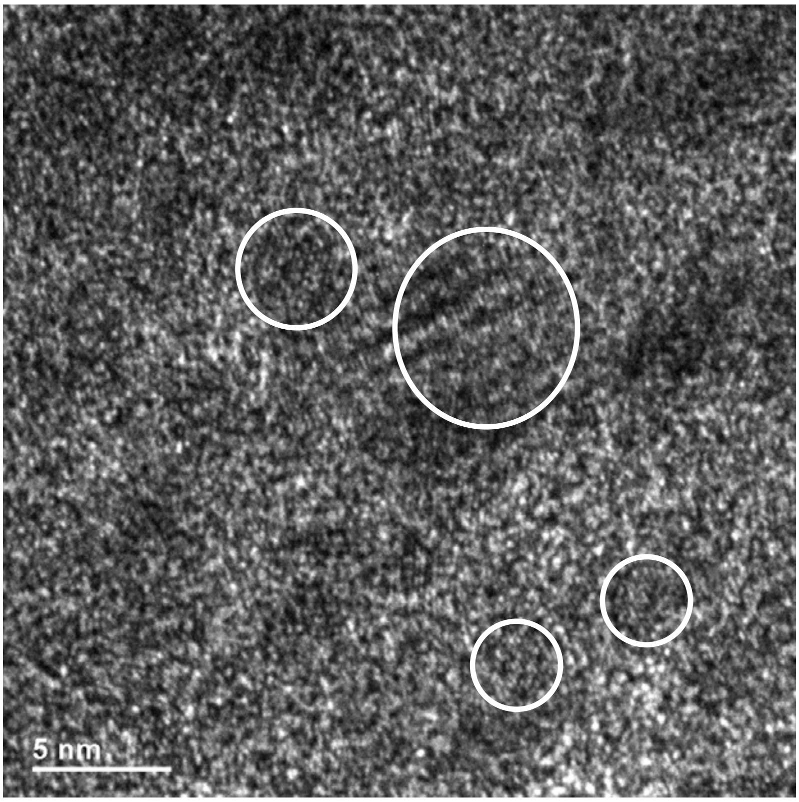

Figure 8.18: HRTEM image of a Ti-DLC film with 25% at. Ti (TiDLC 030610-2) showing a Moiré pattern. Nano-crystallites, which have been circled, appear embedded in the film.

The origin of this spontaneous assembly is not clear, although another study introduced the hypothesis of composition modulation through a catalysis-assisted growth [Wu W.Y., 2004]. A fluctuating kinetic process of the plasma species could also explain this phase separation. On the other hand, *spinodal decomposition* arises as a plausible theoretical background to explain, in general, the arrangement in composite-form, and in our study of Ti-DLC, to justify the formation of multilayers [Corbella C., in press]. Simulations based on this model have been developed in appendix B.

8.4.3. Mo-DLC

Figure 8.19 shows bright- and dark-field TEM images of a Mo film. In comparison with the Ti and W samples, Mo is characterized by a more homogeneous structure. Moreover, the dotted SAED pattern in the inset reveals that the material has been deposited following a crystalline orientation.

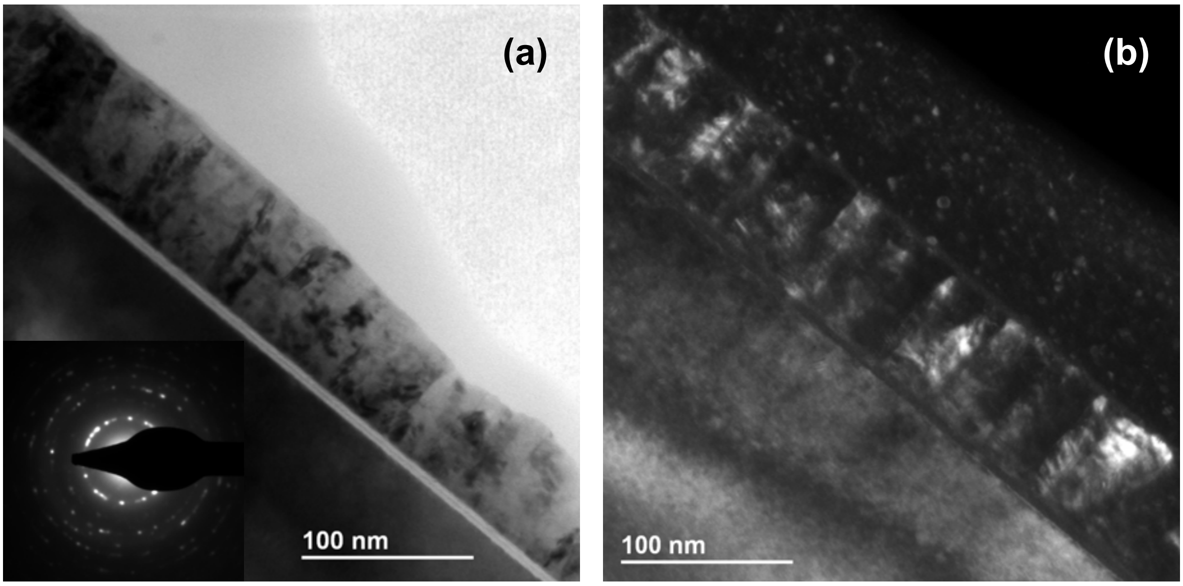

Figure 8.19: The structure of a Mo film (Mo 020628-1) is provided by a bright-field TEM image (a), whereas crystalline distribution is obtained from dark-field observation (b).

The TEM micrographs in figure 8.20 show the evolution of the nanostructure of Mo-DLC. Columns have not been detected therein, but one observes a granular pattern with a density that is reduced as carbon content increases. Similar to W- and Ti-DLC, the SAED diffractograms corresponded to polycrystalline samples and pointed to a weakening of SAED halo as C atoms were added.

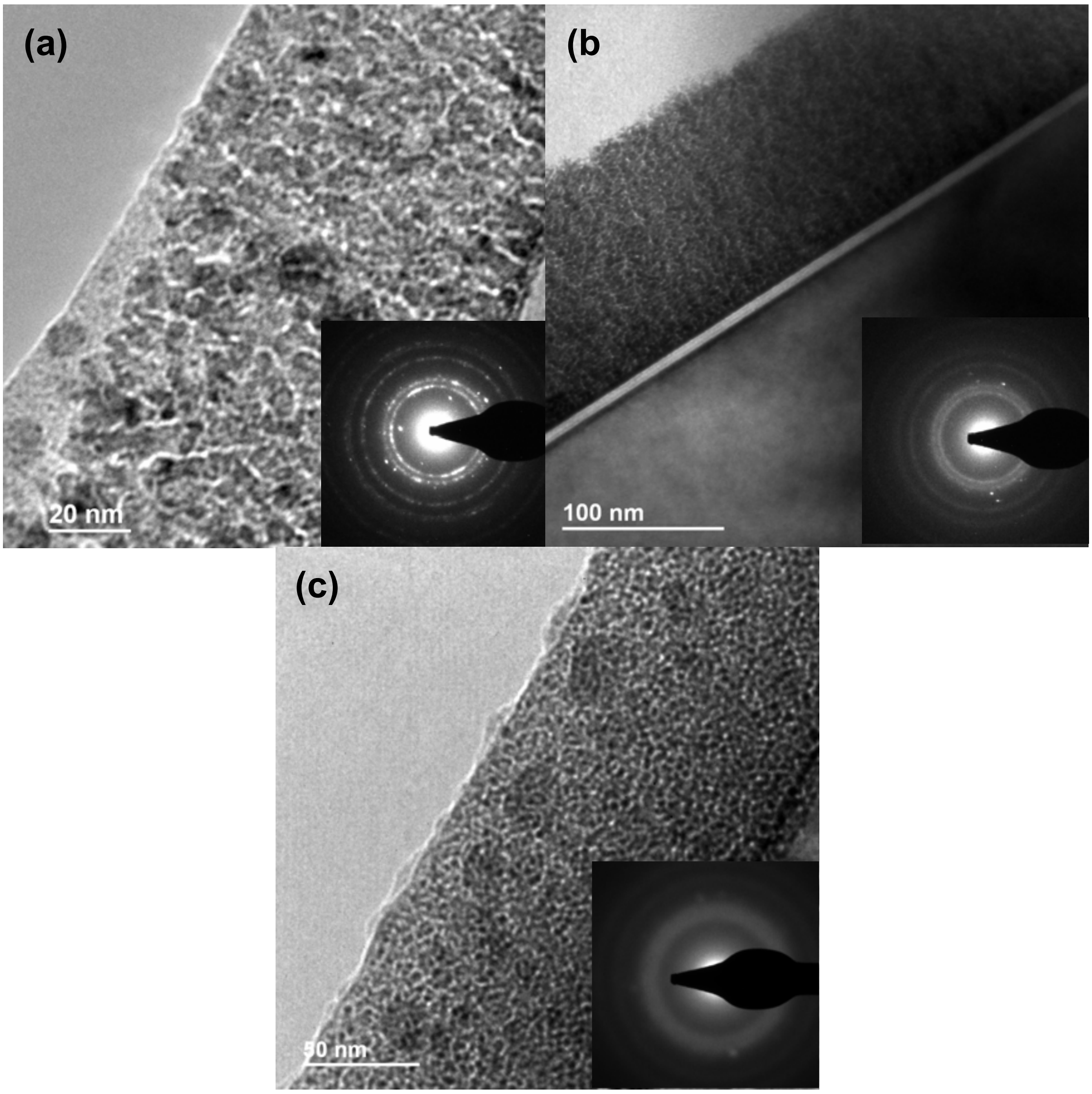

Figure 8.20: Different structures and SAED diffractograms corresponding to Mo-DLC films with R= (a) 3% (MoDLC 020627-2), (b) 6% (MoDLC 030129-1), and (c) 10% (MoDLC 030129-2).

The dark spots distributed throughout the cross-section observed in figure 8.20(c) account for the presence of nano-particles within the film. Moreover, MoC crystallites are embedded within the matrix of these samples. Figure 8.21 shows a HRTEM micrograph of Mo-DLC. The sample exhibits a structure that combines polycrystalline and amorphous phases [Corbella C., 2005c]. Nanometric inclusions identified as MoC crystallites appear embedded in an amorphous matrix. Crystalline domains have about 5 nm diameter, agreeing with the estimations from XRD characterization described in section 8.5.

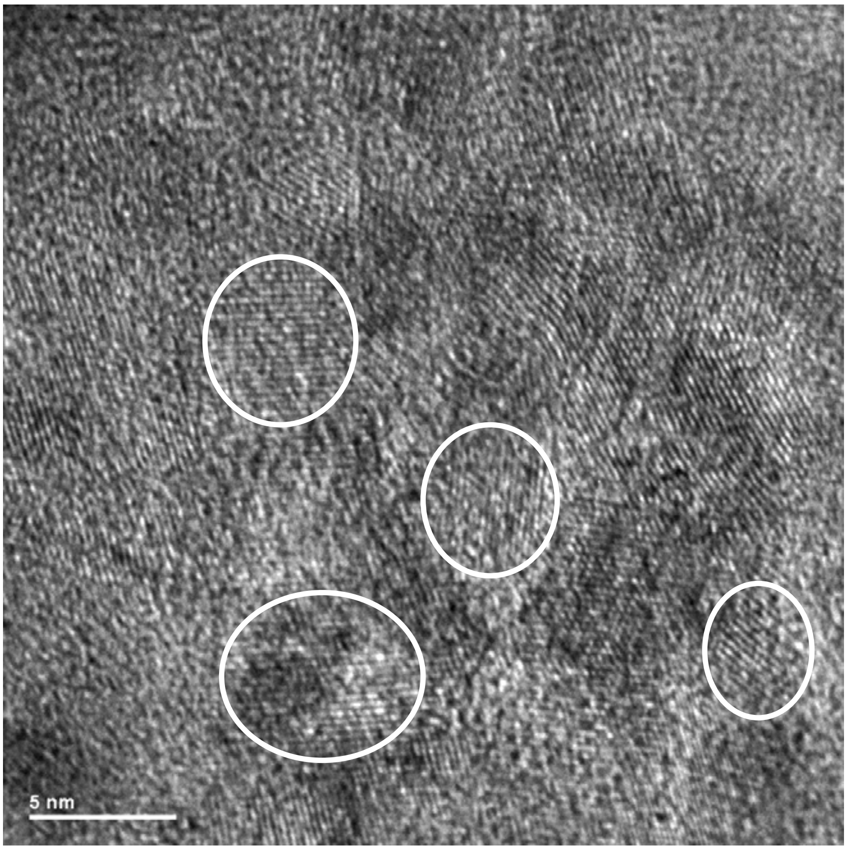

Figure 8.21: Cross-section HRTEM image of a Mo-DLC film with 60% at. Mo (MoDLC 020627-2).

8.4.4. Nb-DLC

Figure 8.22 presents TEM images of Nb-DLC, along with SAED patterns inset, in three stages of C addition. The first micrograph presents a cross-section of a carbon-free Nb film. Its structure is compact and homogeneous, showing crystalline formations with a certain orientation as in the case of the Mo sample.

The next two images evidence a granular growth at R=3%, whereas it turns into columnar as Nb content is reduced down to 8%. A polycrystalline structure persisted even at this high C content.

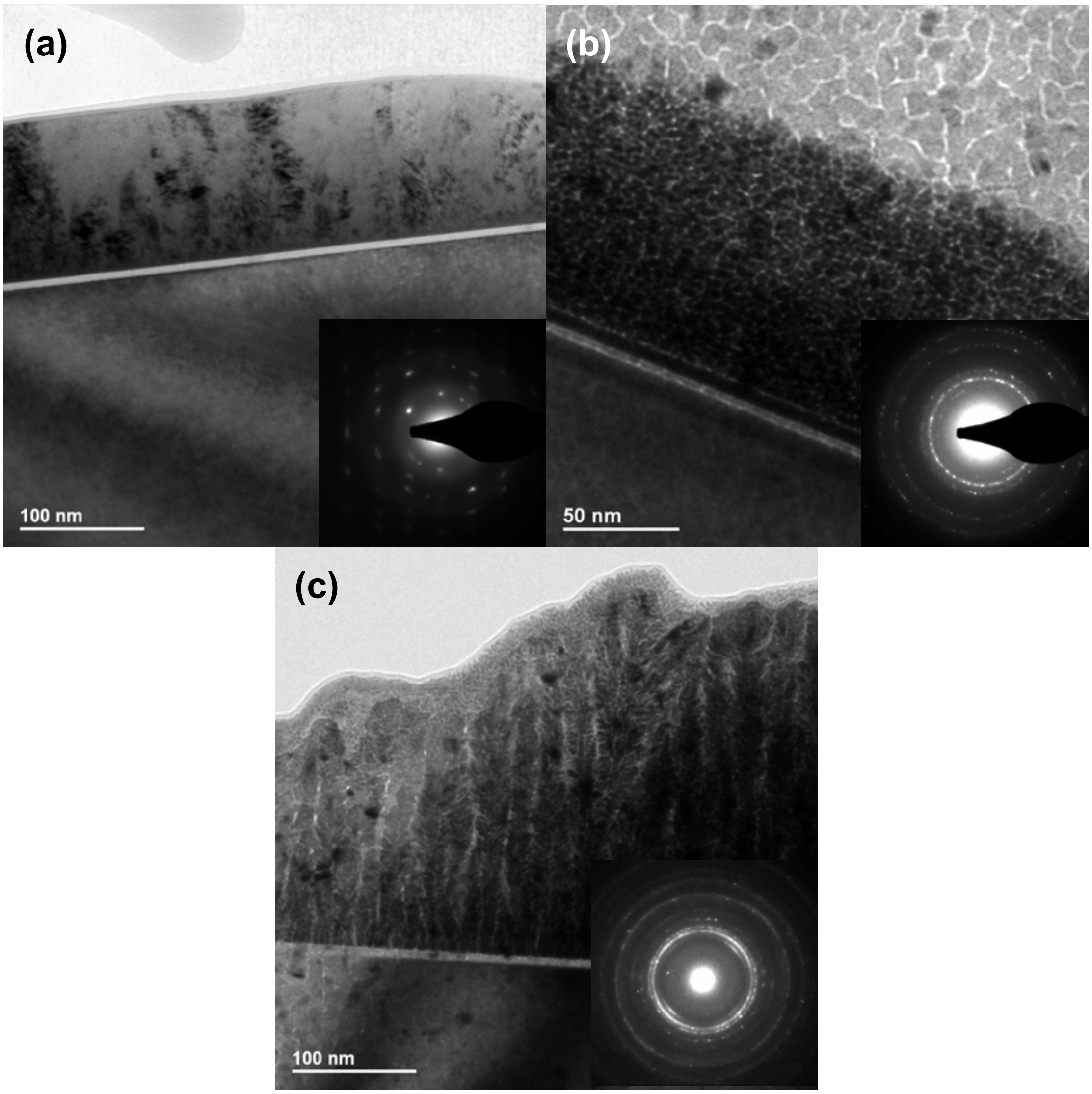

Figure 8.22: Evolution of structure and SAED patterns of Nb-DLC samples with R= (a) 0% (Nb 030116-1), (b) 3% (NbDLC 020716-4), and (c) 6% (NbDLC 030117-2).

8.4.5. Substrate interface

In all the cross-section samples, one can observe a bright layer with sharp interfaces that is located between the substrate and the deposited film. This formation is typical on c-Si substrates, whose surface is spontaneously oxidized in contact with air. This oxide interface is amorphous, as shows the HRTEM image in figure 8.23.

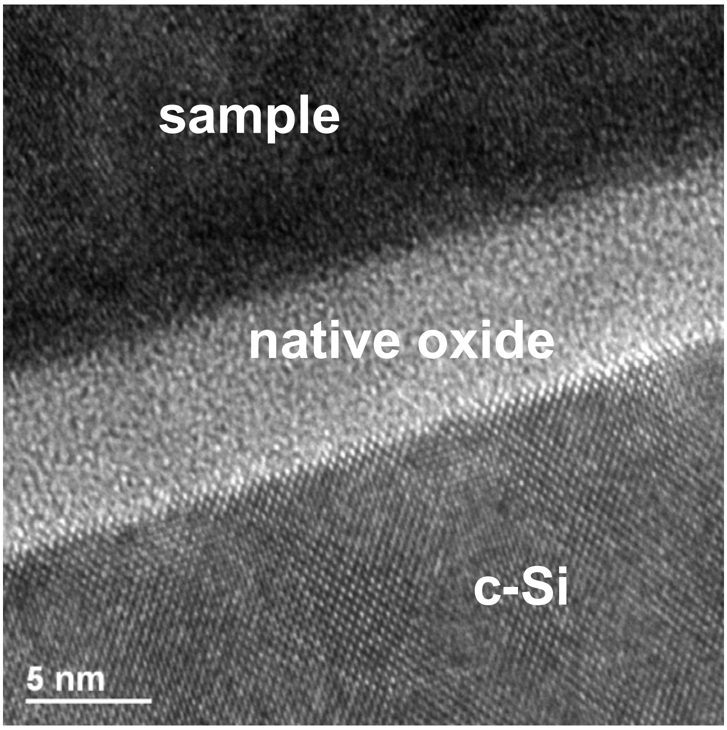

Figure 8.23: HRTEM detail of the oxide layer located between c-Si and a Me-DLC sample (MoDLC 020627-2).

The existence of such interface is indicative of an inefficient cleaning process. Although a cleaning protocol has been applied to all the substrates, a native oxide layer about 5-10 nm thick remains on the surface. Nevertheless, it has not represented a real problem for film growth and adhesion on c-Si substrates.

8.5. X-ray diffraction: microstructure

According to SAED patterns extracted from TEM investigations, the Me-DLC samples consist in amorphous structures containing randomly oriented crystalline metal carbide (MeC) phases. This description is consistent with results published in many papers [Meng W.J., 1998] [Schiffmann K.I., 1999]. In this section, an accurate analysis on crystallinity has been carried out by wide-angle XRD $\theta/2\theta$ scans.

8.5.1. Mo-, Nb- and Ti-DLC

XRD measurements corroborated the presence of cubic MeC inclusions within the Me-DLC films [Corbella C., 2004c]. As commented in chapter 1, the existence of ceramic phases (carbides) instead of isolated metal inclusions supposes a benefit on the mechanical properties of a material, because these ceramic inclusions favour the film hardness. The diffractograms of Mo-, Nb- and Ti-DLC are plotted in figure 8.24, where the evolution of Bragg peaks as a function of metal content is shown. The right most peak is the {100} Bragg reflection due to the monocrystalline silicon substrate. The intensity of this peak could eclipse the contribution of MeC reflections. Thus, this peak has been systematically reduced by tilting the sample in a small angle δ in every XRD scan.

The decrease of metal content in a given series of samples yields to a reduction in peak intensity and to an increase in peak width. The latter parameter is related to the crystallite size, a topic that will be discussed in section 8.5.3.

The Bragg peaks of the diffractograms have been indexed. The Mo-DLC films showed (111), (200) and (220) peaks, which are typical of MoC. These families of crystallographic planes were also found in the Nb-DLC films, which accounted for the presence of NbC crystallites. However, it was necessary to increase statistics in the measurements in order to distinguish the Bragg peaks at low Nb contents. Only clear data from (111) and (200) peaks corresponding to the TiC phase were detected in Ti-DLC. These measurements were performed at low-angle XRD and by increasing the sampling time because of the low signal-to-noise ratio. The necessity of performing a more accurate analysis to reduce noisy data from XRD peaks is indicative of the poor crystallinity of Nb- and Ti-DLC films.

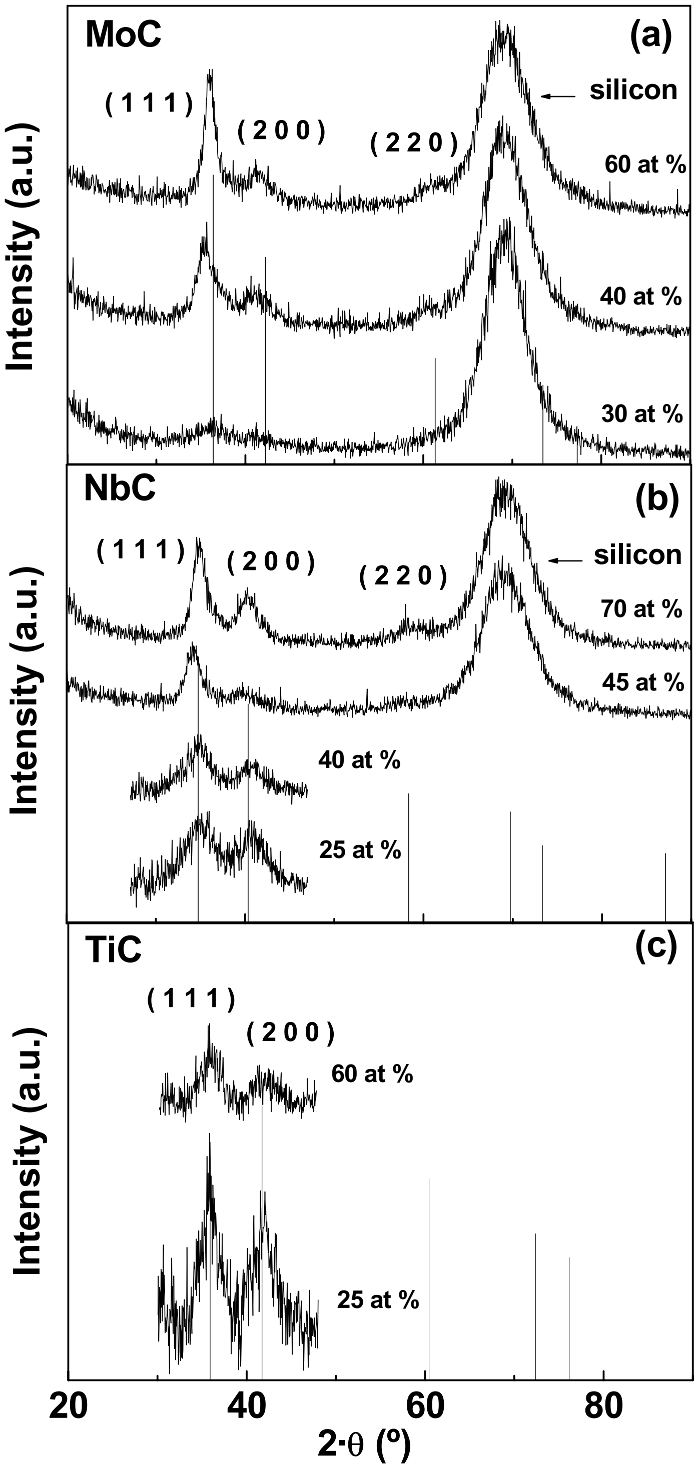

Figure 8.24: XRD diffractograms of (a) Mo-DLC, (b) Nb-DLC, and (c) Ti-DLC films with different metal concentrations.

The cell-size of cubic crystals is determined by the lattice parameter, *a*, which is related to the interplanar distance from Bragg's formula (equation 4.2), d_{hkl}, by the following expression:

$$a = d_{hkl}\sqrt{h^2 + k^2 + l^2} \tag{8.2}$$

where *h*, *k*, and *l* are the Miller's indexes of the considered Bragg peak of a given XRD scan. The lattice parameter has been calculated either from XRD peaks or from SAED rings. Table 8.2 lists the lattice parameters of the Me-DLC samples and shows the concordance of results calculated from both techniques.

8.5.2. W-DLC: coexistence of crystalline phases

The XRD diffractograms corresponding to the W-DLC films are shown in figure 8.25 along with the lines expected for the non-stoichiometric WC_{1-x} phase. These plots present a single peak with an intensity that diminishes as carbon content increases, which is consistent with the SAED patterns and the behaviour presented by the rest of Me-DLC samples (table 8.2).

Some peculiarities can be remarked from the observation of figure 8.25. First of all, the whole XRD diffractogram corresponding to the WC_{1-x} phase has not been measured. The absence of some Bragg reflections from WC_{1-x} crystallites owes to the restriction to crystalline order imposed by the amorphous hydrocarbon matrix [Meng W.J., 1998].

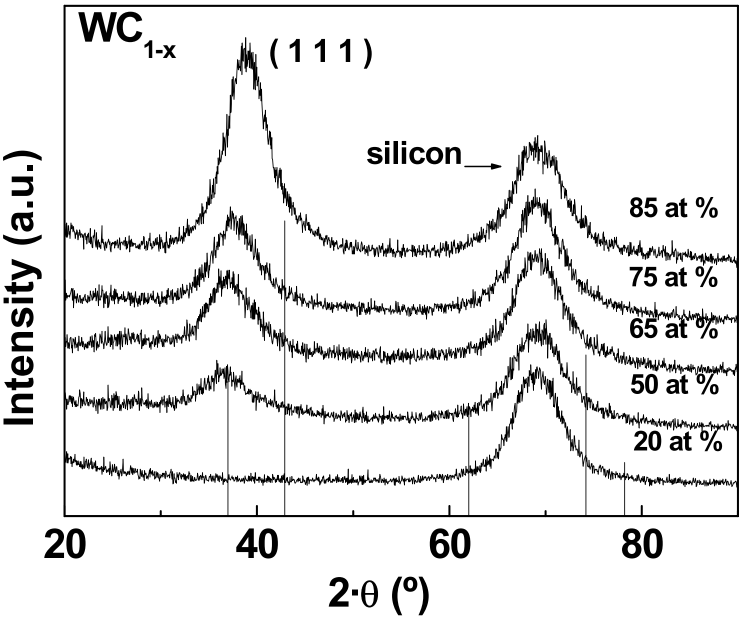

Figure 8.25: XRD diffractogram corresponding to W-DLC films with different metal contents.

Another anomaly is the position-shift of the Bragg peak, which could imply that the lattice parameter increases as the concentration of metal atoms is lowered. This change can be associated to the internal strains in the film. Actually, their influence on the position and width of XRD peaks is used for the study of the residual stress. In the $\theta/2\theta$ scans obtained by the Bragg-Brentano method, one considers the *d*-spacing of the diffraction planes parallel to the film surface. Then, the value of the residual stress is proportional to the relative variation between the *d*-spacing under stressed and relaxed conditions. However, these variations in the crystal lattice are not attributable to the internal stress level, because it is low and independent of carbon content, as shown in section 8.10 [Harry E., 1999].

The variation of lattice parameter can be argued from the coexistence of diverse crystalline phases due to the incorporation of carbon in the W lattice. To corroborate this, the XRD diffractogram of a W film has been measured (figure 8.26). The diffraction peaks reveal clearly the presence of the β-W phase, which consists in a metastable phase of W that lodges small amounts of oxygen [Shen Y.G., 1999]. As expected from the dotted SAED diffractogram, the XRD scan shows a preferential orientation of the {h00} plane, which is perpendicular to the substrate. This preference is highlighted by the relatively high intensities of lines (200) and (400).

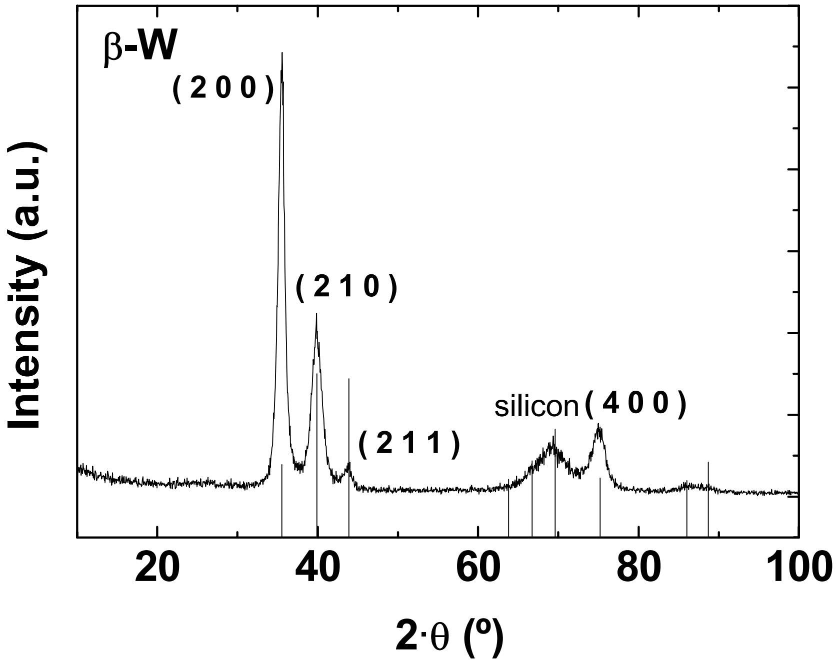

Figure 8.26: The XRD diffractogram of the W film reveals the β-W phase

The gradual incorporation of C in the W matrix, firstly, leads to the cancellation of all the W peaks and to the appearance of a weaker and wider one; and secondly, such incorporation leads to the shift of this peak to lower angles. The single peak can be interpreted as the superimposition of β-W (210) and WC_{1-x} (111) Bragg reflections, since this peak is located between their nominal angular positions. Hence, the metastable β-W phase vanishes at small C abundances, but its (210) reflection still remains and combines in a polycrystalline state with the (111) contribution of WC_{1-x} crystallites at higher C contents.

MATERIAL	% at. Me	a_{XRD} (nm)	a_{SAED} (nm)
Mo-DLC	60	0.4313	0.4328
	40	0.4379	0.4379
	30	0.4292	-
Nb-DLC	70	0.4455	-
	45	0.4546	0.4347
	40	0.4452	0.4453
	25	0.4454	-
Ti-DLC	60	0.4327	0.4488
	25	0.4327	-
W-DLC (suppose WC_{1-x} only)	85	0.4015	0.4004
	75	0.4154	0.4295
	65	0.4211	-
	50	0.4258	-

Table 8.2: Lattice parameters of Me-DLC films calculated from (111) peaks from XRD and SAED patterns.

8.5.3. Crystallite size

The evaluation of the XRD peak widths has provided a lower approximation of the average sizes of crystallites existing in the amorphous matrix of Me-DLC films [Corbella C., 2004c]. Scherrer's formula has been used to estimate the size of the crystallites:

$$D = \frac{0.89\lambda}{B\cdot\cos\theta} \tag{8.3}$$

where D is the crystallite size, λ is the radiation wavelength, B is the full-width half maximum (FWHM) of the diffraction peak, and θ is the Bragg's angle. We have to take into account that aside of the crystallite size, FWHM is also affected by other factors.

Instrumental broadening of the angular width is approximately 0.15°, much lower than the measured one, therefore it can be neglected.

Strains in the network can provide an important source of additional widening. However, the relatively low internal stress of the analysed films has not been considered as a relevant contribution to the peak broadening. Aside of the low stress values (see section 8.10), the crystallite size of Me-DLC films observed in HRTEM investigation did not reach 10 nm. This justifies the legitimacy of using Scherrer's formula, because crystallites smaller than the threshold of around 8 nm broaden considerably the peaks, in the sense that the stress contribution to peak broadening is negligible [Niederhofer A., 1999].

If one deals with non-symmetric XRD lines, more reliable data about *D* can be obtained by considering the integral peak-width instead of FWHM in equation 8.3. In this thesis, FWHM value of the peaks was used instead of integral peak-width because Bragg reflections showed a symmetric shape.

Figure 8.27 shows the evolution of the MeC crystallite size vs. the metal-to-carbon atomic ratio. The crystallite size grew monotonically with metal content from 0 in the DLC case up to 6 nm, except for W-DLC films, where this size saturates at 2 nm.

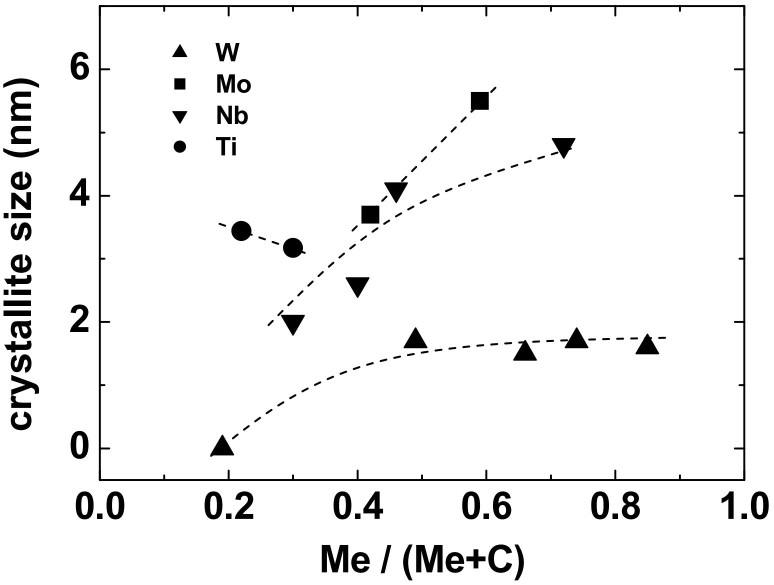

Figure 8.27: Plot of crystallite size (XRD) as a function of the chemical composition of Me-DLC films. The smallest particles correspond to the W-DLC samples.

The W-DLC samples contain crystallites with a constant diameter close to 2 nm, excepting the film deposited at R=25%, where no XRD signal was registered. Specifically, two regions can be observed in figure 8.27 in the case of W-DLC films. The first one corresponds to layers with low metal concentration, where an increase of metal content increases the particle size. That is in agreement with previous works [Schiffmann K.I., 1999]. The second region, which is extended from 50% at. W to metallic films, shows that crystallites do not grow as the chemical composition is varied. This implies that the density of inclusions in the matrix increases. The saturation of the crystallite diameter could be attributed to the existence of a critical size.

A general decrease of the particle size is observed as the melting point of the corresponding metals increases: 3695 K, 2896 K, 2750 K and 1941 K for W, Mo, Nb, and Ti, respectively. In fact, higher melting points limit the mobility of the metal atoms during deposition. Then, the formed crystallites are smaller because the reduced mobility makes difficult the aggregation of surface diffusing atoms.

8.6. Surface properties: roughness and wettability

In this section, the surface roughness of the Me-DLC films has been studied by AFM. As in the case of pulsed-DC DLC films, RMS roughness is shown to depend on the deposition parameters, namely *R*, which determines the metal concentration. Wettability has been parameterised by contact angle with water, which has been measured by Wilhelmy plate method and sessile drop technique, being discussed the results from both techniques.

8.6.1. Surface roughness

The tribological properties of the coatings depend on the surface roughness. Therefore, films with very flat surfaces are desirable for protective coatings applications. The surface topography of Me-DLC films is influenced by metal content. Concretely, we can distinguish three different stages in metal concentration of W-DLC samples if we attend to surface roughness, as shows figure 8.28:

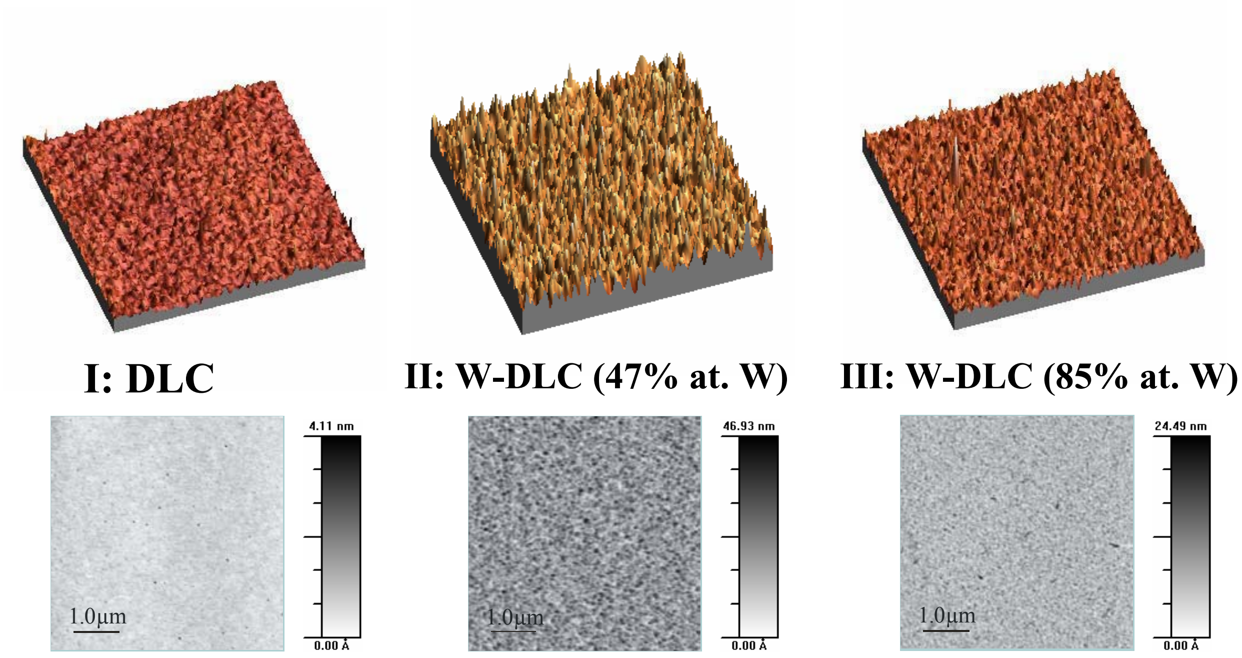

I: DLC **II: W-DLC (47% at. W)** **III: W-DLC (85% at. W)**

Figure 8.28: Surface topography of AFM scans in a 5 x 5 µm^2 square of W-DLC films with different metal contents: isometric and planar views.

The dependence shown by W-DLC can be extrapolated to a general behaviour for the other metals. Figure 8.29 shows the influence of composition on surface topography, detecting RMS roughness values of the order of the crystallite sizes shown in section 8.5. The smallest RMS roughness values are 0.19 and 0.21 nm, and correspond to W-DLC (R=25%) and DLC films, respectively. In general, surface roughness values of metal-rich and carbon-rich films are similar, while intermediate values of composition define a maximum. The deposited W-DLC films have for example an RMS value of 5.86 nm at approximately 50% at. W; regarding Nb-DLC, it was 4.00 nm at 47% at. Nb. Both materials show the highest roughness among the four metals, suggesting that their columnar growth promotes roughening.

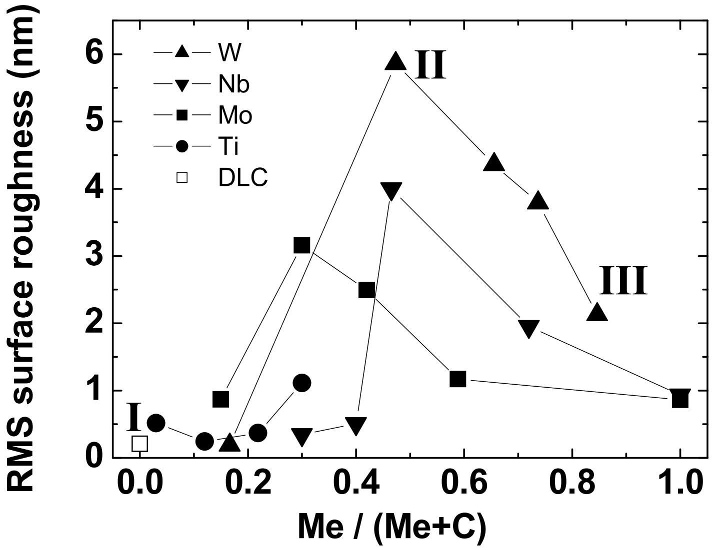

Figure 8.29: RMS surface roughness, calculated from AFM measurements, vs. chemical composition. All the elements point generally to a maximum of roughness at a given composition. The numbers I, II and III label the samples shown in figure 8.28.

The low roughness of metal-rich films could come from a smoothing effect due to a re-sputtering mechanism promoted by the major argon bombardment [Peng X.L., 2001]. The similar roughness values calculated at lowest metal concentration are indicative of identical compositions at surface according to SIMS results (section 8.3), where a smooth DLC layer is formed. Then, the maximal roughness exists in the region where both smoothing mechanisms are inefficient, i.e. far from extreme values of metal concentration. A third motor for surface roughening consists on the major presence of *sp*^{2} bonds in Me-DLC films [Zhang P., 2002]. Some recent models assume that metal atoms within a DLC matrix act as catalysts in the formation of *sp*^{2} sites: each embedded metal carbide nanoparticle is surrounded by a *sp*^{2}-rich boundary, which is in contact with the amorphous DLC matrix [Bewilogua K., 2004].

8.6.2. Wettability

The motivation of this characterisation is to prepare coatings showing very low interaction with liquids, in order to minimise their degradation in wet conditions. Figure 8.30 plots the contact angle vs. the composition of Me-DLC films. These are measurements of the "dynamic" contact angle, because they were performed by the Wilhelmy plate method.

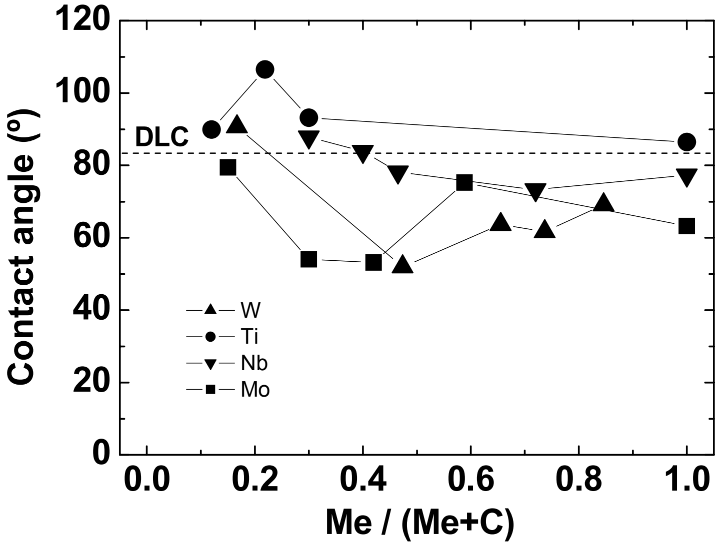

Figure 8.30: Variation of the contact angle with the composition of Me-DLC samples, measured by the Wilhelmy plate method.

These results suppose an approach to surface energy. Thus, the highest hydrophobicity is achieved at low metal contents, as expected from the hydrophobic character of DLC. In all the cases, the contact angle is higher than 50º. Ti- and Nb-DLC samples show the lowest wettability, overcoming 100º of contact angle. However, irregularities observed in the shape of advancing-receding loops lead to considerable uncertainties in the evaluation of this parameter.

The sessile drop technique is an optical method to determine the contact angle. As shows figure 8.31, Me-DLC films tend to minimise the contact angle as the metal content increases. This trend is clearer with this technique because it is more accurate, presenting less data-dispersion than operating with the Wilhelmy plate method. Contact angle values range up to 86º, which is lower than the upper limit observed with dynamical contact angle. The drop method usually provides an overestimation of contact angle due to an effect of contamination on interacting surfaces.

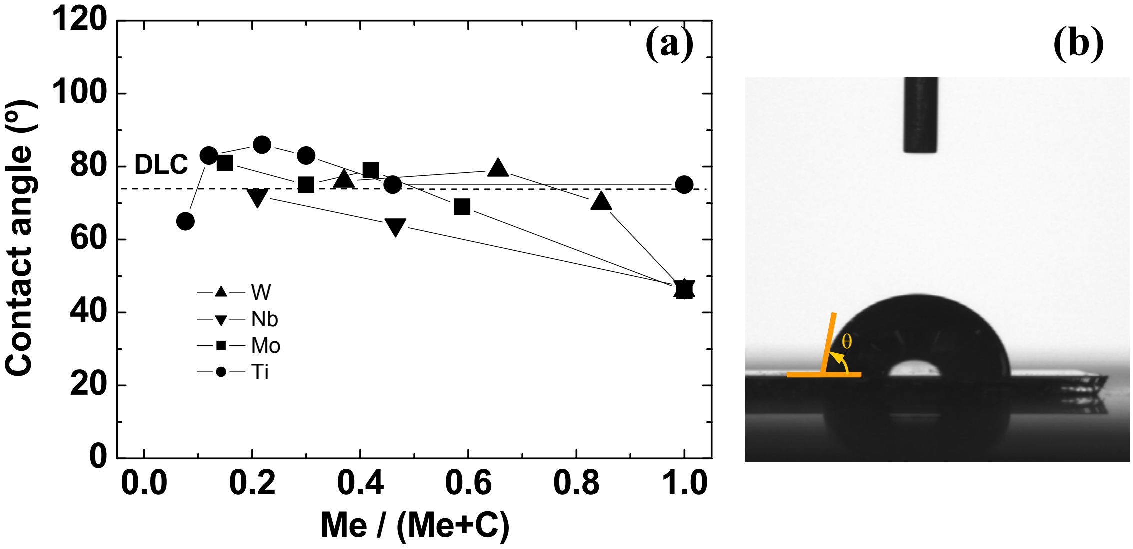

Figure 8.31: (a) Monitoring of the Me-DLC wettability by means of the sessile drop method, and (b) detail of a water drop on a Ti-DLC film.

8.7. Scanning electrochemical potential microscopy

SECPM provides electrochemical potential mappings on a conductive surface with nanometric resolution. Surface images of a W-DLC film (65% at. W) in figure 8.32 show a granular appearance. The grains that show the greatest contrast are about 30 nm size, and the registered pattern is similar to an AFM scan.

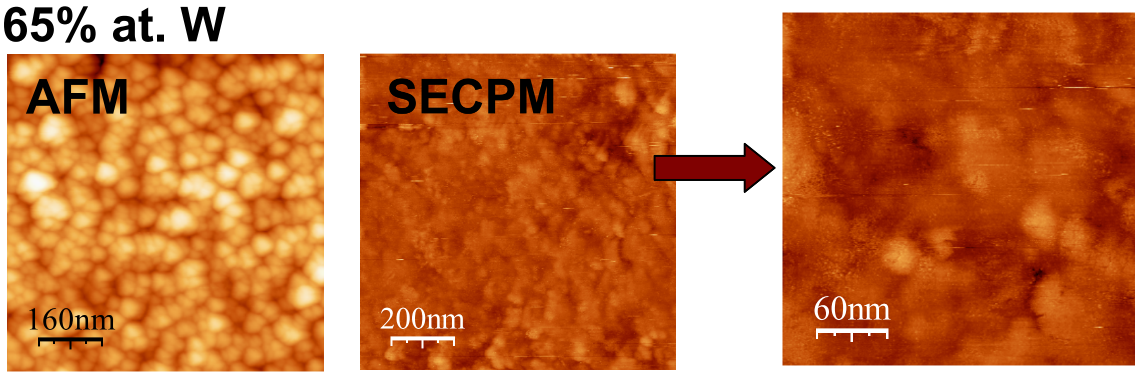

Figure 8.32: Mapping of the electrochemical potential over the surface of W-DLC 65% at. W.

Figure 8.33 shows a SECPM image of a W-richer film (85% at. W). Here, the higher metal content seems to yield greater equipotential surfaces, whereas AFM measurements account for a non-altered structure if compared to the carbon-richer sample. Therefore, a clustering of metal islands is inferred from this technique, which supposes a new method to scan the metal distribution on the surface of conductive samples in addition to conductive-AFM technique (c-AFM) [Corbella C., 2005c].

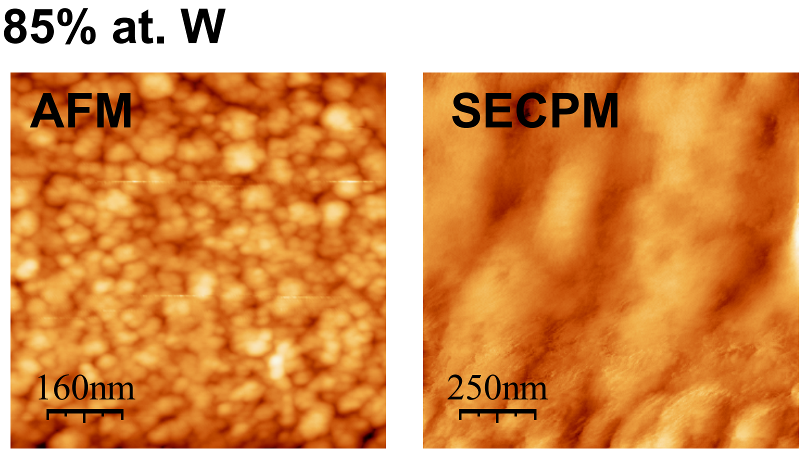

Figure 8.33: Mapping of the electrochemical potential over the surface of W-DLC 85% at. W.

The lateral resolution can be improved by bringing the potentiometric probe to the film surface, which is achieved by increasing the concentration of the electrolyte. This operation owes to the change of potential profile created by the electrically charged surface of the sample in a liquid medium. According to Gouy-Chapman model of the electrochemical double-layer, the potential within the medium decreases much more drastically when ionic strength increases. Therefore, it is easier to keep the probe closer to the surface when ionic strength increases, thus achieving a better resolution.

We note that measurements carried out in a 0.1 M solution and applying more than 0.2 V to the sample lead to a severe surface oxidation and thus become a destructive technique. Therefore, SECPM mappings were performed by using H_2O_{mq}. The applicability of this technique is restricted to metal-rich surfaces because insulating materials obviously cannot operate as electrodes.

8.8. Optical properties

One of the main issues in Me-DLC research is the improvement of the mechanical performance, which depends on the metal used and the way that it incorporates into the film. The full understanding of the relationship between film structure and properties remains nowadays as an open subject. Concerning optical characterization, ellipsometry in the visible and IR domains appears as a reliable and highly sensitive technique to clarify this issue.

Me-DLC films show in general a diversified optical behaviour in the range of energy from 1.5 to 4.1 eV measured by a multichannel rotating analyser ellipsometer. Since RMS roughness values are lower than 6 nm, the films present an ideal optical surface, flat and smooth. However, the whole structure of the films is the system roughness/film/substrate, which is optically represented by the complex pseudo dielectric function, $\langle\tilde{\varepsilon}\rangle$. This variable is obtained from ψ and Δ by assuming a semi-infinite media structure. Then, the spectroscopic complex pseudo refractive index, $\langle\tilde{n}\rangle$, can be calculated from the $\langle\tilde{\varepsilon}\rangle$ spectra.

In figure 8.34, the real part of $\langle\tilde{n}\rangle$, $\langle n\rangle$, of the metallic samples (R=0%) has been represented in the energy range from 1.5 to 4 eV. One spectrum corresponding to a pure DLC films is also represented. When CH_4 is incorporated to the growth process, the optical properties evolve from the characteristic values of the metallic samples to these of a DLC film [Corbella C., 2004a].

Especially interesting is the case of the optical absorption. The absorption coefficient spectra, α, of the series of W-DLC, obtained from $\langle\tilde{\varepsilon}\rangle$, are represented in figure 8.35. For this metal, the sample obtained with R=1% presents an increase from the value of the pure metal sample. When CH_4 flow ratio increases from 1%, the optical absorption decreases and the films become more transparent. In this case, the oscillations observed in the low energy range correspond to the interferences with the substrate. The Nb-, Ti- and Mo-DLC films show a gradual decrease of the optical absorption.

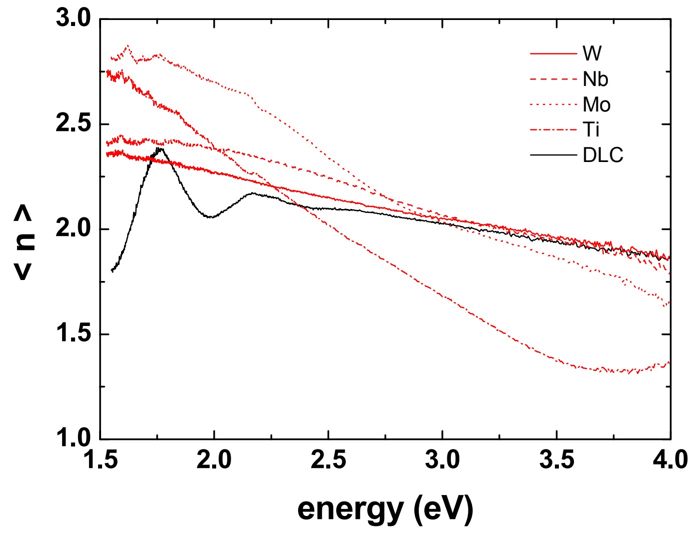

Figure 8.34: Real part of pseudo refractive index, $\langle n \rangle$, spectra in the visible range of pure metallic samples (Mo, Nb, Ti and W) deposited without CH_4 addition. The typical spectrum of a DLC film is also represented.

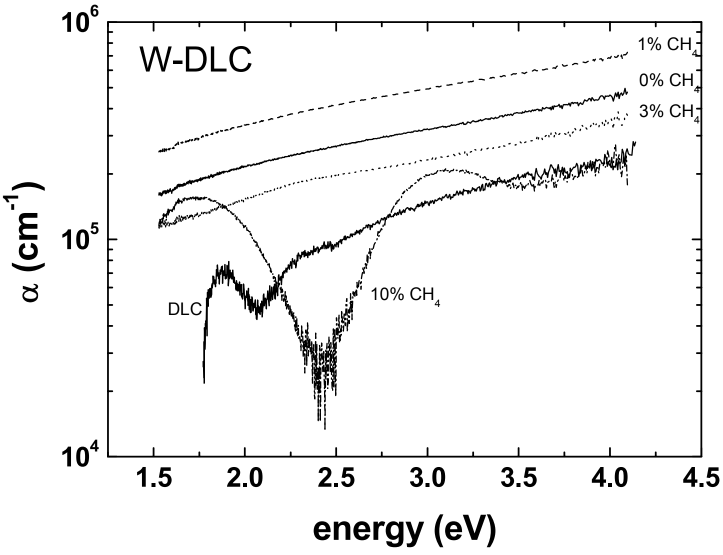

Figure 8.35: Absorption coefficient, α, spectra in the visible domain obtained from the pseudo dielectric function, of W-DLC samples deposited on c-Si substrates at different R. The corresponding values of a DLC film are also plotted.

Between 3 and 10% of CH_4 flow ratio, a clear change from an absorbing to transparent character is detected. It is associated to the abrupt decrease of the nanocrystallite size corresponding to the change from a metal dominated matrix to a DLC dominated one.

In general, the films have a high absorption coefficient in this range, between 10^5 and 10^6 cm^{-1}. Films containing Nb and Ti correspond to a Sellmeier absorbent model having two resonances far from the measured range. Films containing W and Mo exhibit an exponential absorption front in the energy range from 1.5 to 4.1 eV:

$$\alpha(E) = \alpha_g \exp\left(\frac{E - E_g}{E_0}\right) \tag{8.4}$$

where E_0 is the characteristic energy of the Urbach edge, E_g is the extrapolated optical band-gap energy, and α_g is the optical absorption coefficient at the band-gap energy.

Figure 8.36 shows the evolution of α_g with the CH_4 dilution in Ar during the deposition process by reactive magnetron sputtering from the corresponding metal targets. The decrease of α_g indicates an increase of the transparency of the samples as the carbon content increases into the films. The trend to a low absorption of the films is related to the deposition conditions, and particularly to the low substrate temperature and to the ion bombardment conditions, which favour the deposition of polymeric carbon.

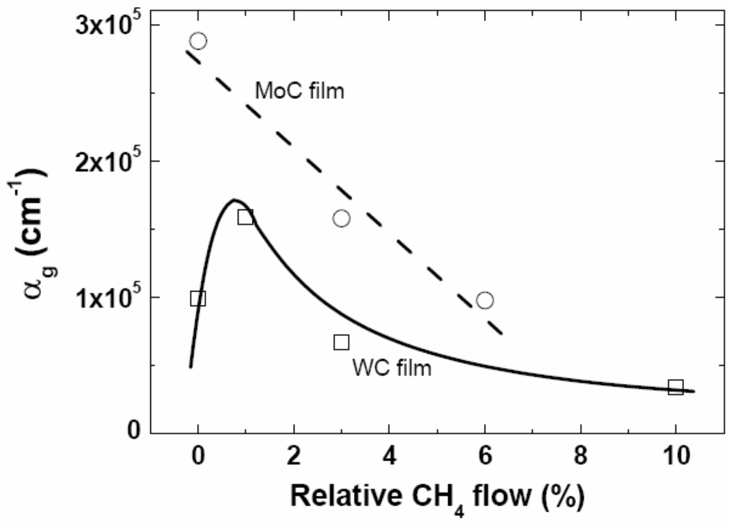

Figure 8.36: Plot of optical absorption coefficient at the band-gap energy, α_g, of the Mo- and W-DLC films as a function of R.

The evolution of the Urbach edge energy as a function of R is shown in figure 8.37. This parameter, which takes a value approximately 2 eV for all the samples, controls the slope of the absorption edge and is related to the interband transition probability. The lowest slope of the Urbach edge corresponds for Mo-DLC sample to R=3% and for W-DLC sample to 1%. If we assume that high values of E_0 are associated to disordered networks, the results shown in figure 8.37 indicate a process of higher disorder of the matrix at low carbon contents, probably related with the transition from a metallic network to a carbon network.

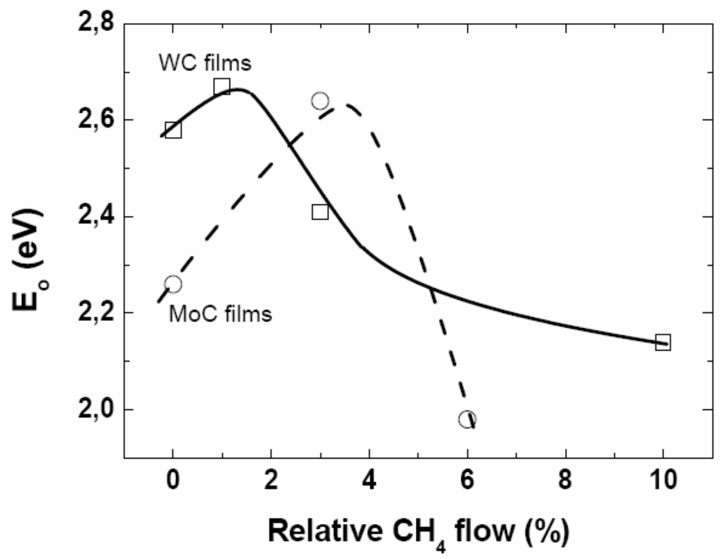

Figure 8.37: Plot of Urbach edge energy, E_0, of the Mo- and W-DLC films as a function of *R*.

The gap energy estimated using the Urbach edge model, E_g, has a weak dispersion for all the samples of each series. Series of W-DLC films have a gap energy of 0.020 eV, higher than the series of Mo-DLC (E_g=0.015 eV). The shift of this value to lower energies for Mo-DLC films could be related to the lower atomic radius of Mo. The very low values of the gap energies for both series of samples are probably connected to an absorption by free electrons. Moreover, the identical values of gap energy for pure metal films or Me-DLC films indicate a dominant optical behaviour related to the metallic character.

Figure 8.38 shows ψ spectra of a series of Nb-DLC films deposited on gold substrates. In the IR domain, the lowest values of ψ were obtained for the metallic sample (R=0%), and it can be seen that they coincide with the visible ones. As *R* increases, films become more transparent and ψ values approach to these of gold substrates.

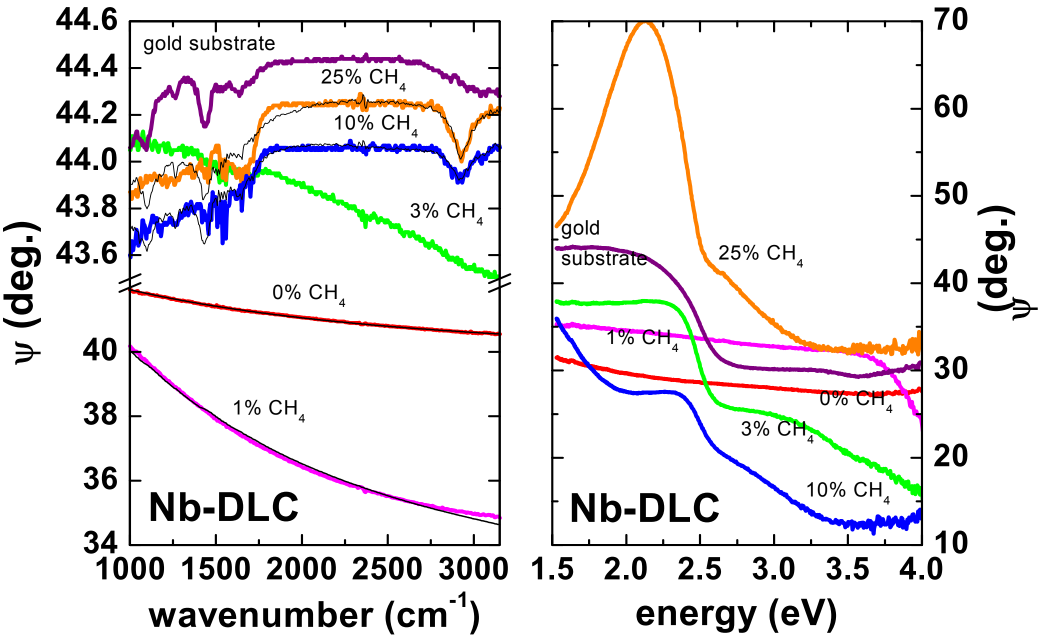

Figure 8.38: IR and visible ψ spectra of a series of Nb-DLC films deposited on gold substrates. Continuous thin lines correspond to the fit obtained by considering a mixture of a metallic reference and a transparent medium.

In order to model the optical response of the film-substrate structures, we considered for the Me-rich films the Drude model for free electrons:

$$\varepsilon(\omega) = \varepsilon_\infty + \frac{\omega_p{}^2}{-\omega^2 + i\Gamma_D\omega} \tag{8.5}$$

where ε_∞ is the high frequency dielectric constant, ω_p is the plasma frequency and Γ_D is the phenomenological damping parameter. The model used for the more transparent samples considered a mixture of the dielectric properties of the Me-rich sample and a transparent medium described by using a classical model with two oscillators:

$$\varepsilon(\omega) = \varepsilon_\infty + \sum_{j=1}^{2} \frac{(\varepsilon_0 - \varepsilon_\infty)\omega_{0j}{}^2}{\omega_{0j}{}^2 - \omega^2 + i\omega\Gamma_{Lj}} \tag{8.6}$$

where ε_∞ and ε_0 are the high and the low frequency dielectric constants, respectively, ω_{0j} are the vibration frequencies and Γ_{Lj} are the phenomenological damping parameters.

Continuous thin lines in figure 8.38 correspond to the fit obtained by considering a mixture of a metallic reference following the Drude model with $\varepsilon_\infty = 1$, $\omega_p = 9.7$ and $\Gamma_D = 0.595$, and a transparent medium with $\varepsilon_\infty = 1.95$ and two oscillators at 2900 and 2920 cm^{-1}.

8.8.1. Optical gap from Tauc's plot

Tauc's plot obtained from spectroscopic ellipsometry and transmittance measurements provided the optical gap energy of the films. Ellipsometric measurements fit well for a film with high α, but in the case of low α and/or thinner films multiple interferences appear, which made the analysis difficult. Transmittance measurements were performed in this latter case. The optical gap energy, E_{gap}, is calculated from the Tauc's dependence:

$$(\alpha \cdot E)^{1/2} = B(E - E_{gap}) \tag{8.7}$$

where α is the absorption coefficient, E is the photon energy, and B is a constant factor.

Figure 8.39 shows the evolution of the optical gap with respect to the composition of the films. The values range between 0 and 1.4 eV, converging in all the cases to the gap value of pure DLC, 1.2 eV.

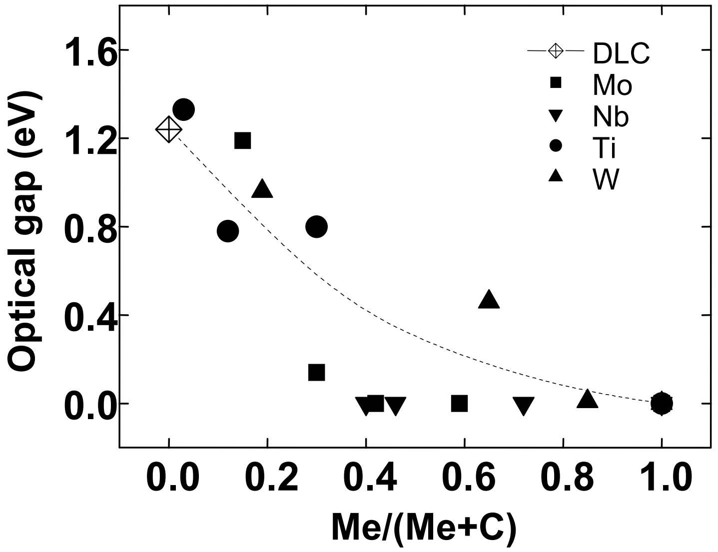

Figure 8.39: Optical gap vs. chemical composition of Me-DLC films. All the values tend to DLC gap at low metal contents.

In general, the optical gap of the metal-rich films increases smoothly parallel to the carbon content and the evolution depends on the metal. W- and Ti-DLC show a gradual decrease of the optical gap when the metal content increases, whereas Mo- and Nb-DLC show there an abrupt decrease.

8.9. DC electric conductivity

The incorporation of metals into DLC modifies the electric properties of this hard material. Thus, the electric conductivity of Me-DLC films appears correlated to their metal content. Like optical characterization, the composition of Me-DLC has been studied by monitoring a functional parameter, which in turn informs us about structural properties.

The electrical conductivity, σ, at room temperature of the W-DLC films was measured at different W concentrations by the four-point probe method (figure 8.40). Its value for a pure W film is approximately 10^5 S/m. The reduction of the conductivity by increasing the carbon content is expected because of the semiconducting properties of DLC [Staryga E., 2005].

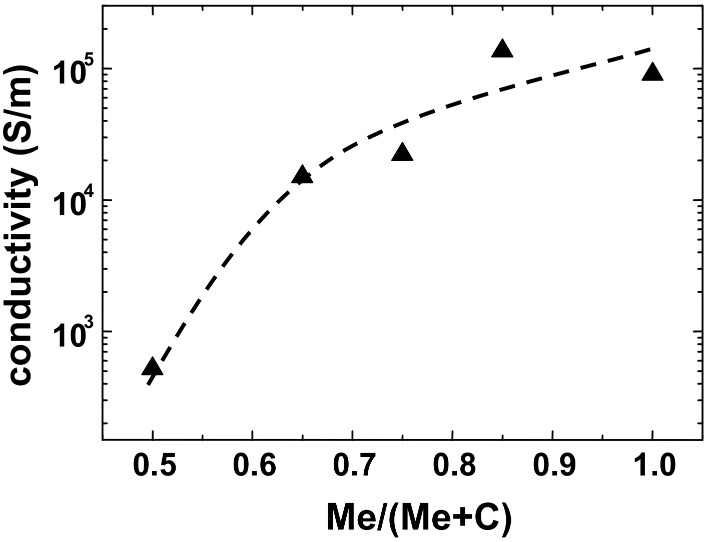

Figure 8.40: Electric conductivity of W-DLC films as a function of W abundance.

A value of W conductivity in bulk form higher than 10^7 S/m has been reported. The reason of the increased resistivity of this W film accepts two explanations. First, this increase could mainly come from the formation of an oxide surface layer. Since W presents a high reactivity with oxygen, this oxidation may be produced during film deposition and/or after the process [Rusli, 2001]. Chemical analysis by XPS has shown a significant oxygen presence on surface of W-rich films. There, oxygen atomic ratios up to 20% corresponding to the O(1s) signal have been registered. The presence of this metal oxide layer results anyway in a conductivity decrease.

Another possible contribution to the reduction of conductivity in the W film is the measurement set-up. The electric current employed for resistivity measurements flowed parallel to the substrate, i.e. orthogonal to the W columns observed in the TEM study of section 8.4. Hence, column boundaries could reduce the electron mobility in the planar direction and, thus, the conductivity becomes lower. This hindering of electric current can be explained in terms of microscopic parameters for an ohmic material:

$$\sigma = n \cdot e \cdot (v/E) \tag{8.8}$$

where n is the electron density, e is the fundamental charge, v is the drift velocity and E is the electric field. The ratio v/E is called *mobility*, and limits the current density. In our case, the conductivity at high metal content is enhanced by an increase of charge carriers. However, it saturates at 10^5 S/m owing possibly to a decrease of electron mobility.

Measurements of electric resistance at different temperatures were carried out [Corbella C., 2005a]. The *R(T)* characteristic provides the thermal activation energy of the film. Its value is related to the arrangement of energy bands in the case of a semiconductor, and it gives an intuitive idea of the necessary energy to enhance the conductivity of the material:

$$\sigma = \sigma_0 \exp\left(-\frac{E_a}{kT}\right) \tag{8.9}$$

where σ is the electric conductivity, E_a is the activation energy, k is the Boltzmann constant, and T is the temperature.

The Arrhenius plots of conductivity of figure 8.41 show that the semiconductor behaviour of W-DLC films is enhanced at higher carbon concentrations, whereas a nearly constant conductivity is observed in W-rich films. Indeed, the sample with 20% at. W shows a thermally activated conductivity, in the range of 1 S/m, almost four orders of magnitude lower than the sample 65% at. This temperature-dependent behaviour is the dominant conduction mechanism at high temperatures for Me-DLC [Huang Q.F., 2000].

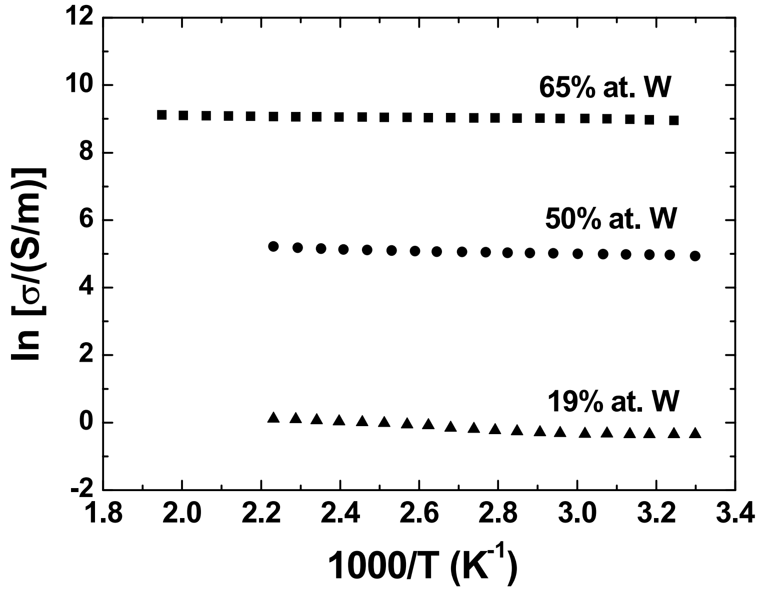

Figure 8.41: Arrhenius plots of W-DLC samples with different metal content.

Figure 8.42 shows the dependence with W abundance of the activation energy, E_a, defined by the Arrhenius formula (equation 8.9). The activation energy is calculated from fitting the measured conductivity values to the Arrhenius expression. Approximately 6 meV were measured in the W-rich film, and 53 meV in the case of 20% at.W. A similar behaviour was registered by Rusli et al. [2001].

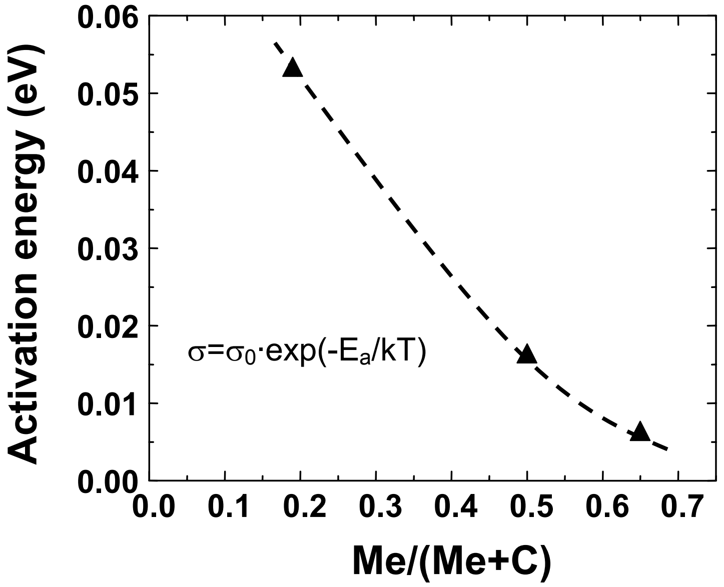

Figure 8.42: Activation energy vs. W abundance calculated from the Arrhenius plot of conductivity of W-DLC films from room temperature to 526 K.

8.10. Mechanical and tribological properties

8.10.1. Intrinsic stress

The variation of the mechanical stress in the Me-DLC films with the relative CH_4 flow is shown in figure 8.43. In general, we observe that DLC suffers a stress reduction when metals are added [Corbella C., 2004c], evidencing thus a significant improvement in the film adhesion.

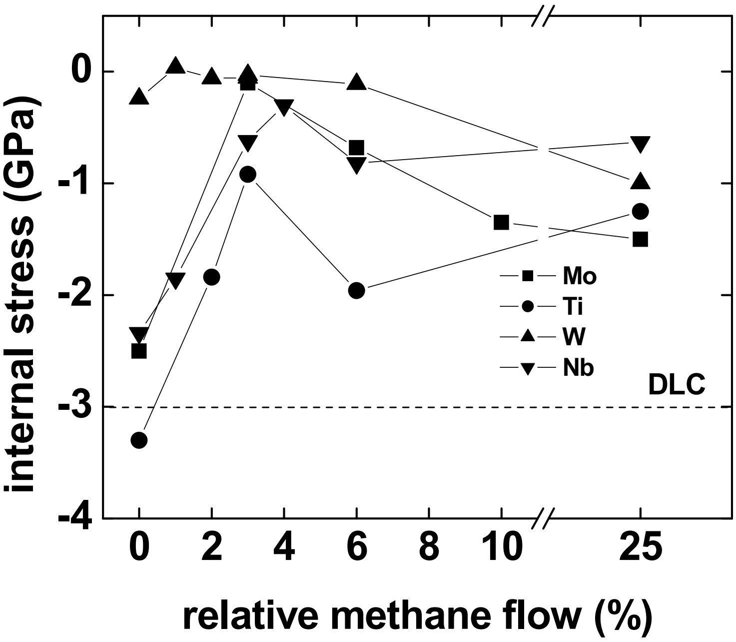

Figure 8.43: Variation of compressive stress of Me-DLC films as a function of *R*.

The sputter-deposited metal films show a compressive stress of approximately 3 GPa as a consequence of the negative biasing of the substrates (-200 V). The incorporation of methane in the gas mixture first leads to a reduction of the compressive stress below 1 GPa for all the metals. In particular, the W and Mo containing samples show practically no stress when R=3%.

As *R* increases to values greater than 3%, the compressive stress slightly increases until it reaches values close to 1 GPa at R=25%. These compressive stress values are lower than that of DLC films (3 GPa). This behaviour corresponds to metal-doped DLC films, whose stress is expected to be significantly lower than DLC because the new structure has a more relaxed configuration. Me-DLC samples prepared at R=25% are three times less stressed than DLC. Although these films only exhibit DLC phase by XPS, they are grown on a thin metallic layer, as reported by SIMS in section 8.3. These metal formations act as buffer layers, contributing thus to film relaxation.

The coincidence of the stress minima at R≈3% for all the Me-DLC films suggests that the preparation parameters have a relevant influence on the mechanical properties of the films. Indeed, the stress increase below and above R=3% could be related to an effect of intense Ar bombardment (PVD regime) and strains in the amorphous hydrogenated carbon matrix (PECVD regime), respectively.

The stress variations in Me-DLC are ascribed to structural changes as the metal content varies. For instance, the very low stress of W-DLC films is closely related to the nanostructure imposed by W. The columnar structure of W films leads to a low-stressed material, even more relaxed when dendrites are formed [Shen Y.G., 2000]. The persistence of this structure, even with considerable carbon contents as shown in section 8.4, leads to such relaxed structures. In the case of Ti-DLC, the stress release seems to be associated to the spontaneous formation of interfaces between the components. In this way, the periodic self-assembly in Ti/C bilayers could induce a reduction of the overall compressive stress with a mechanism similar to the observed in W/a-C multilayers studied in chapter 7.

The size of crystalline domains in Me-DLC plays also an important role in film stress. If we attend to the MeC crystallite sizes plotted in figure 8.27, we observe that this size and stress appear correlated. Samples containing smaller crystalline inclusions become less stressed, as in the case of W-DLC (≈ 2 nm), whereas Mo-, Nb- and Ti-DLC films contain bigger crystallites (> 2 nm) and their stress is higher (figure 8.44).

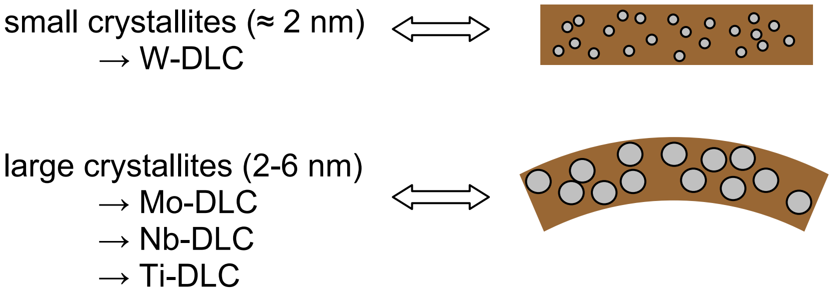

Figure 8.44: The compressive stress of Me-DLC films is correlated with the size of crystalline domains.

The stress reduction in films with small crystallites can be interpreted as a consequence of a toughness enhancement by an effect of nanostructure. Although the ideal toughening consists on hindering the crack initiation and propagation, grain boundary sliding also promotes it. For a sample containing small inclusions, a considerable strain release may be achieved through a major density of grain boundaries, which confers more plasticity but softens simultaneously the film [Schiotz J., 1998]. Furthermore, a crystallite size reduced to nanoscale lowers the stress because crack size is approximately proportional to grain size [Zhang S., 2005].

8.10.2. Micro-scratch

Friction coefficient and critical load parameters have been obtained by applying micro-scratch tests to Me-DLC films. Figure 8.45 shows the variation of friction coefficient vs. applied load during scratch tracks performed on different samples. The critical load was higher than 20 N in some cases. Although there is not a clear relation with deposition conditions because this parameter depends strongly on film thickness, these results suggest an acceptable film adhesion to substrate.

Figure 8.46 compares the results from different tests, and shows low friction coefficients for all the Me-DLC samples. Their values are below 0.1, and Nb- and W-DLC films improved the tribological properties of DLC, which has a friction coefficient of about 0.05. Concretely, W-DLC exhibited a coefficient below 0.03. These coefficients have been evaluated as the average value of friction coefficient along a scratch track. Then, error bars of the order of 0.01 should be considered.

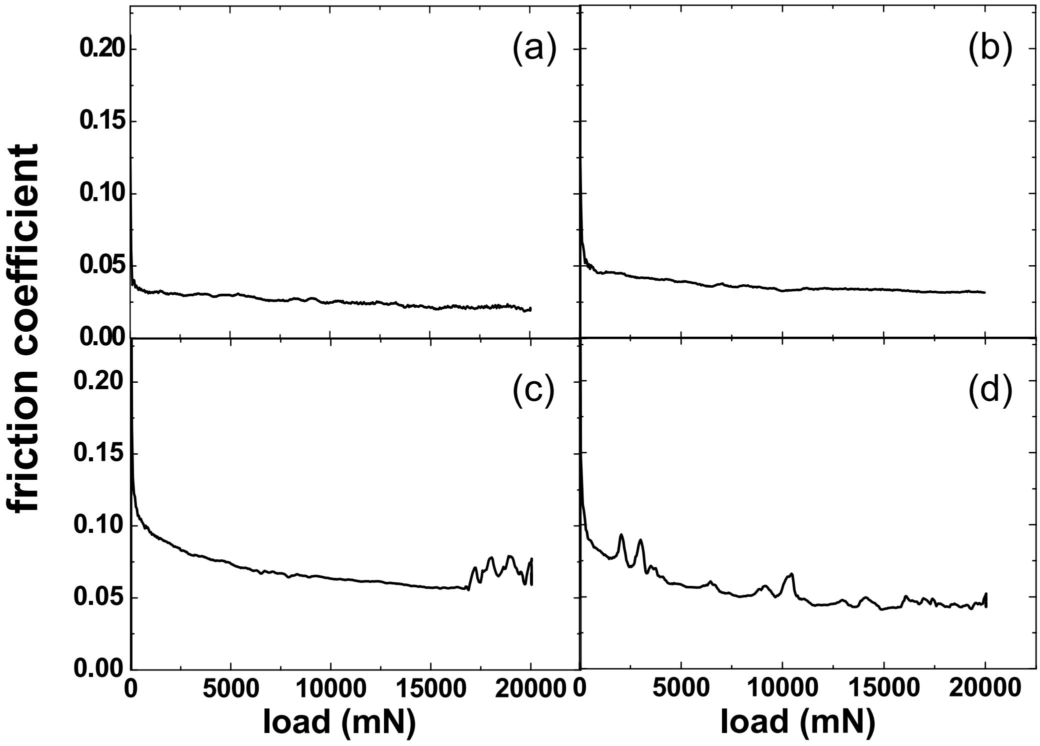

Figure 8.45: Friction coefficient as a function of applied load in micro-scratch tests on (a) W-DLC (WDLC 030121-1), (b) Mo-DLC (MoDLC 030129-2), (c) Ti-DLC (TiDLC 030128-1), and (d) Nb-DLC (NbDLC 020716-3).

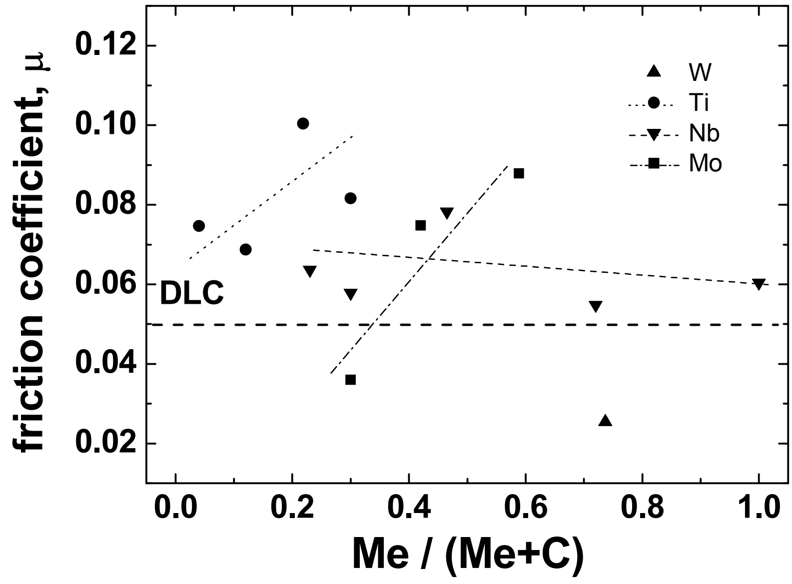

Figure 8.46: Influence of the metal content on the friction coefficient of Me-DLC films. The value corresponding to DLC is marked by the dashed line.

8.10.3. Hardness

Nanoindentation tests provided an estimation of the hardness of Me-DLC films. These samples are very thin, most of them below 300 nm thick. Thus, most of these results are underestimated because of the substrate (c-Si) influence. A solution consists on considering only the most superficial data in hardness vs. indentation depth plots. There, only a few data are plotted, contributing to enlarge the error bars (~ ±1 GPa).

Figure 8.47 shows that hardness of the Me-DLC samples is far to be constant. Instead, hardness weakly tends to minimise at intermediate metal concentrations. This behaviour is clearly exhibited by the W-DLC films, which occupy the most widespread range of composition values. Such evolution leads to a range in hardness values between 8 and 22 GPa; note that the DLC hardness is not reached in any case (24 GPa). This behaviour can be an effect of microstructural rearrangements of DLC matrix lodging MeC nanoparticles. As commented in section 8.6, the incorporation of metal atoms has a reported collateral effect on *sp^3/sp^2* ratio. A predominance of graphitic (*sp^2*) clusters reduces the carbon hardness and leads to surface roughening [Zhang P., 2002]. The coincidence in hardness minimum and roughness maximum agrees with this argument.

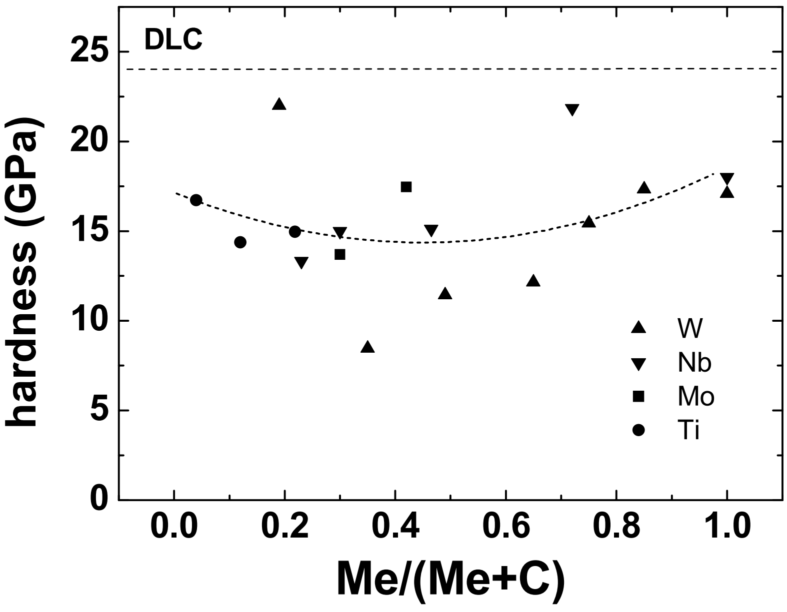

Figure 8.47: Evolution of hardness of the Me-DLC films vs. their metal concentration.

In conclusion, the combined deposition of DLC and metals improves basically the film adhesion and the friction coefficient. Enhancements of hardness for the optimization of Me-DLC mechanical properties may be achieved by depositing thicker films, say ~ 1 μm thick.

Summary and conclusions

1) Films of metal containing DLC (Me-DLC) have been produced by reactive magnetron sputtering using pulsed-DC power from different metal targets (Mo, Nb, Ti, W) and RF bias using different gas mixtures of methane and argon.

2) The properties of the films have been changed from a metallic behaviour to a DLC one by varying the methane flow rate from 0 to 25%. XPS, EPMA and SIMS measurements show that the Me-DLC samples are generally uniform in composition, excepting carbon-rich samples.

3) The structure of the Me-DLC films changes with metal and its content, as verified by TEM analysis. W- and Nb-DLC show typically a columnar growth, Ti-DLC is spontaneously structured in multilayers and Mo-DLC has a granular pattern. Cross-section HRTEM images reveal that the Me-DLC structures consist on a distribution of nanocrystallites embedded in an amorphous matrix.

4) SAED and XRD scans account for the formation of metal carbide nanocrystallites. Their density and size (up to 6 nm) show a decrease when carbon is in abundance, owing to a progressive predomination of amorphous DLC in C-rich samples.

5) For each metal, the RMS surface roughness is of the order of the nanocrystal size and achieves a maximum at intermediate compositions. The maximum of contact angle is around 80º and decreases smoothly as the metal content is higher. SECPM images reveal a non-homogeneous metal distribution on the surface, variable with composition.

6) From the analysis of UV-visible and IR spectroscopic ellipsometry measurements, it can be seen that the optical properties of the films were switched in a wide range from a metallic behaviour to a DLC one. The optical gap is found to increase as the metal content is reduced, up to DLC usual values.

7) W-DLC samples exhibit a thermally activated conductivity, whose activation energy increases with carbon content.

8) The film-substrate adhesion of Me-DLC has been improved due to a reduction in compressive stress (< 0.1 GPa for W-DLC), thanks to the new structures introduced by each metal. The friction coefficient (< 0.03) is lower than the corresponding to PECVD DLC, and the critical load overcomes 20 N. Hardness values range from 8 to 22 GPa, being inferior than DLC hardness (24 GPa).

9) The wide variety of film structures provides interesting properties to Me-DLC. All these results show that the prepared Me-DLC films are suitable for surface coatings applications requiring low roughness, moderate hydrophobicity and low friction coefficient.